RSC Advances

ROYAL SOCIETY OF CHEMISTRY

PAPER

View Article Online
View Journal | View Issue

Check for updates

Cite this: *RSC Adv.*, 2025, **15**, 39369

3D printing of hydrogels: a synergistic approach of rheology and computational fluid dynamics (CFD) modeling

Siraj Ahmad, Hatif Alam and Prachi Thareja *

Received 19th June 2025
Accepted 2nd October 2025

DOI: 10.1039/d5ra04380h

rsc.li/rsc-advances

The development of printable hydrogel inks with optimized rheological properties is critical for advancing extrusion-based 3D printing. In this study, we present a systematic investigation of kappa-carrageenan (κCG) hydrogel inks formulated with and without 10 mM KCl and gold nanoparticles (AuNPs) to assess their printability, flow behavior, and structural performance. All formulations exhibited shear-thinning behavior, characterized using the Power Law model, while stress sweep measurements provided insights into viscoelastic moduli and yield stress. Inks without KCl displayed smooth flow and superior single-layer printability but lacked multi-layer stability, while KCl-crosslinked inks showed enhanced mechanical stability and structural retention in multi-layer constructs. The ink containing both KCl and AuNPs demonstrated the best results in multi-layer printing, combining the mechanical stability imparted by KCl with enhanced shear-thinning behavior from AuNPs. CFD simulations using ANSYS fluent were employed to estimate extrusion pressures and visualize shear rate distributions within the syringe–nozzle geometry. Using CFD results, the thixotropic protocol was modified to reflect actual shear conditions during printing. Inks without KCl showed high viscosity recovery, while those with KCl exhibited lower values, likely due to sample slippage at high shear. Despite this, KCl-containing inks showed excellent multi-layer printability, indicating effective structural recovery. Complementary FTIR, XRD, thermal, and FESEM analyses validated structural and morphological features of inks. This integrated experimental–CFD framework offers a predictive approach to understand hydrogel ink behavior, highlighting the interplay between formulation, flow properties, and print performance. The findings provide a foundation for next-generation bioinks for tissue engineering and soft material applications.

Introduction

Kappa-carrageenan (κCG) is a naturally derived polysaccharide obtained from certain species of red seaweed, such as *Kappaphycus alvarezii*.[1] Over the past decade, κCG has attracted growing interest as a hydrogel-forming material, particularly for biomedical and pharmaceutical applications due to its ability to form strong, thermoreversible gels in the presence of potassium (K^+) ions.[2,3] The gelation process arises from the ionic interaction between the negatively charged sulfate groups of κCG and K^+ ions, which stabilize the double-helical conformation and promotes the formation of intermolecular junction zones, thereby strengthening the three-dimensional network[4] The unique molecular structure, composed of alternating 3-linked β-D-galactose-4-sulfate and 4-linked 3,6-anhydro-α-D-galactose units, with sulfate groups attached, gives it a high degree of hydrophilicity and allows it to interact with a range of biological molecules.[2] The incorporation of gold nanoparticles (AuNPs) into the κCG hydrogel matrix will lead to an increase in the biological activity, as well as the antioxidant and antitumoral properties.[5] AuNPs are also capable of interacting with κCG chains through electrostatic attraction with sulfate groups and hydrogen bonding with hydroxyl groups, which can influence the polymer microstructure and, in turn, modulate the viscoelastic properties of the resulting gels[6] One of the major advantages of incorporating AuNPs into κCG hydrogels is that it enhances their photothermal properties. κCG hydrogels embedded with gold nano-bipyramids have demonstrated efficient photothermal conversion, making them suitable for photothermal therapy. For instance, a κCG-gelatin hydrogel containing carvacrol-loaded gold nano-bipyramids was developed for prostate cancer treatment *via* fractionated photothermal-chemotherapy, highlighting the potential of such systems in biomedical applications.[7] The presence of AuNPs also affects the mechanical and rheological behavior of κCG hydrogels. Their incorporation can influence gelation kinetics and improve structural integrity, which is critical for 3D printing applications. The use of AuNPs in κCG hydrogels has shown applicability in nanophotonics, photothermal therapy, and imaging.[8] In terms of biological function, κCG hydrogels having AuNPs have been explored for antimicrobial and

Department of Chemical Engineering, IIT Gandhinagar, Palaj, Gandhinagar, 382355, India. E-mail: prachi@iitgn.ac.in

anticancer effects.[9] The surface characteristics of AuNPs support interactions with microbial membranes, enhancing antimicrobial action. Injectable chitosan/κCG hydrogels with AuNPs have also improved cell adhesion and proliferation, suggesting potential in tissue engineering applications.[10] Additionally, the incorporation of AuNPs imparts enhanced electrical conductivity and contributes to the development of hydrogel-based biosensors. These AuNPs facilitate electron transfer, resulting in improved performance of devices like non-enzymatic glucose sensors, where free-standing AuNPs-loaded hydrogels have shown promising results.[11] Altogether, the incorporation of AuNPs into κCG hydrogels extends their utility across photothermal therapy, tissue engineering, biosensing, antimicrobial, antitumoral, and anticancer treatment, offering a multifunctional platform based on a biocompatible matrix.

One of the most appealing features of κCG hydrogels is their resemblance to the natural extracellular matrix (ECM) found in human tissues.[12] Because of their high-water content and soft, flexible structure, κCG hydrogels can support cell adhesion and proliferation, making them suitable as scaffolds for tissue engineering. For example, when κCG is blended with other biopolymers such as chitosan or gelatin, the resulting composite hydrogels have been shown to promote osteogenic differentiation in bone tissue engineering models.[13] Moreover, their gelling properties can be tailored by adjusting the ionic environment or by introducing chemical crosslinkers, allowing us to fine-tune the mechanical strength and degradation rate of the hydrogel to suit specific biomedical applications.[14] Seliktar *et al.* also showed that the high biocompatibility of κCG hydrogel ensures a safe interaction with the living tissues.[15] The κCG hydrogel's inherent biocompatibility and mild gelation process make it especially attractive for use in sensitive tissue environments.[16] Drug delivery is another area where κCG hydrogels have shown significant promise.[17] The negatively charged sulfate groups on κCG chains can form electrostatic complexes with positively charged drugs or proteins, resulting in stable encapsulation and controlled release profiles.[18] For instance, κCG has been used to formulate microspheres and nanogels for the sustained delivery of antibiotics, anti-inflammatory agents, and even anticancer drugs.[19] Bardajee *et al.* demonstrated how the blending of κCG with other polymers such as alginate, polyvinyl alcohol (PVA), or acrylic acid will lead to the formation of hybrid hydrogels with improved mechanical properties and tailored drug release behavior.[20] Beyond these core biomedical applications, κCG hydrogels are also found to be useful in other fields. In environmental science, for instance, κCG based materials are used for the adsorption of heavy metals and dyes from wastewater due to their ion-exchange capacity.[21]

With the advent of 3D printing technologies, it has become possible to fabricate intricate structures designed specifically for biomedical applications, including tissue engineering, drug delivery, and regenerative medicine. Among various biomaterials explored for 3D printing, κCG has garnered significant attention due to its favorable gelation properties, biocompatibility, and structural similarity to glycosaminoglycans present in the extracellular matrix.[22] Kamlow *et al.* developed κCG emulsion gels incorporating sunflower oil and evaluated their printability using extrusion-based 3D printing, highlighting the potential of κCG in fabricating complex structures for personalized food applications.[23] With the addition of KCl salt, the storage modulus (G') of κCG hydrogels increase, thereby enhancing the mechanical properties and improving multilayer printability.[24] Stavarache *et al.* formulated a marine-derived polysaccharide blend of κCG and sodium alginate, producing scaffolds with controlled architecture suitable for tissue engineering.[25] A study by Kumari *et al.* introduced methacrylated kappa-carrageenan (MA-κCG) suitable for digital light processing (DLP) 3D printing, demonstrating outstanding printability and potential for fabricating intricate biomedical devices.[26] This highlights the versatility of κCG as a biocompatible ink, capable of forming hydrogels with tunable mechanical and rheological properties suitable for various 3D printing applications.

In extrusion-based methods such as robocasting, direct ink writing (DIW), and bioprinting, printability is not defined by a single factor but spans several levels. At the most basic level, it refers to extrudability, meaning the ability of an ink to pass through the nozzle under applied pressure in a continuous and stable manner, without clogging or breaking.[27] Once extruded, printability also reflects the extent to which deposited filaments can maintain their intended geometry and build stable multilayered structures, rather than spreading or collapsing.[28,29] In biofabrication, the concept goes further, since extrusion conditions directly influence biological outcomes. Shear stresses during extrusion and the rate at which the ink recovers its microstructure determine the rate of cell survival, proliferation, and differentiation.[30,31] Therefore, the optimization of printability requires a balance between rheological properties and processing parameters with structural fidelity, while also limiting biological damage. For hydrogels such as κCG, this broader understanding of printability becomes particularly important.

Computational fluid dynamics (CFD) has emerged as a powerful tool in the field of extrusion-based 3D printing, particularly for the simulation of hydrogel behavior during extrusion. By numerically solving the Navier–Stokes equations, CFD allows for detailed analysis of fluid flow, pressure distribution, velocity profiles, and shear stress, which are considered to be the parameters critical for optimizing the printability and performance of bioinks. Among various platforms, ANSYS fluent is widely used due to its robust capabilities in simulating complex non-Newtonian flows that are typical in hydrogel printing processes.[32] CFD plays a crucial role in reducing experimental trial and error by providing quantitative insights into how different ink formulations behave under flow. Simulations using ANSYS fluent can accurately predict how these inks respond to changes in geometry, boundary conditions, and flow rates, thereby helping to fine-tune printing parameters for better shape fidelity and reduced material wastage.[32,33]

CFD also serves as a powerful tool for predicting wall shear stress profiles in different nozzle geometries and sizes, which is particularly relevant for optimizing extrusion-based bioprinting systems. By simulating flow behavior under various design configurations, CFD enables the identification of critical regions within the printing geometry that may be prone to excessive shear stress. These results are essential when tailoring nozzle dimensions to strike a balance between print resolution, extrusion pressure, and cell viability.[34] Additionally, CFD studies can help estimate local shear rates experienced by the material during printing, which can then be used to design the thixotropy recovery experiments and yield stress assessments. For κCG inks, this approach ensures that experimental setups closely mimic real-world printing conditions, ultimately leading to more relevant and reproducible rheological evaluations.[35]

In this study, κCG-based hydrogel inks were prepared with structural modifications introduced through KCl crosslinking and the incorporation of AuNPs. Their rheological response was examined through flow curve analysis, frequency sweep, strain sweep, and model fitting to evaluate shear-thinning and yield stress behavior, followed by 3D printing tests to assess both single-layer and multi-layer print fidelity. In addition, the inks were characterized using FTIR to confirm chemical interactions, XRD to assess crystallinity and structural organization, FESEM to observe microstructural morphology, and TGA/DSC to evaluate thermal stability. To complement the experiments, CFD simulations were carried out to estimate extrusion pressures, visualize internal flow patterns, and quantify shear distributions within the nozzle. The simulated shear rates were further applied to refine thixotropy measurements, allowing a more accurate assessment of structural recovery under conditions relevant to printing. Through this combined approach, the study aims to establish how formulation parameters influence the printability of κCG inks and to provide a framework that links rheology, flow simulations, and structural recovery for the design of biocompatible hydrogel systems.

Materials & methods

Sample preparation

To prepare pristine κCG hydrogel (1.5% (w/v)), 150 mg of kappa carrageenan powder (Sigma-Aldrich, USA, CAS Number 11114-20-8, 788.66 g mol^{-1}) was taken and mixed with 10 ml of deionized (DI) water, and then stirred in a water bath maintained at 70 °C at 800 rpm for 2 hours until all the κCG powder is completely dissolved. To prepare ionically crosslinked κCG hydrogel (1.5% (w/v)), 150 mg of κCG powder was dissolved in 10 ml of 10 mM potassium chloride (KCl) solution, while the remaining procedure is same.

For the *in situ* synthesis of AuNPs in pristine as well as crosslinked κCG hydrogel, 150 mg of κCG powder was dissolved in 10 ml of DI water (for pristine hydrogel), or 10 ml of 10 mM KCl solution (for crosslinked hydrogel) and the aqueous mixture was heated up to 70 °C in a water bath under continuous stirring at 800 rpm. Subsequently, 1 ml of 1.52 mM gold(III) chloride trihydrate ($HAuCl_4 \cdot 3H_2O$) (Sigma-Aldrich, USA) was added to the aqueous mixture of hydrogel when the temperature of the water bath reached 70 °C, and then the mixture was allowed to stir at 800 rpm and 70 °C for 24 hours. The synthesis of AuNPs within the hydrogel matrix after 24 hours was confirmed by UV-visible spectrophotometry. Finally, the hydrogels were left at room temperature to cool down for 24 hours before further use.

A schematic diagram (Fig. 1) illustrates the reduction of Au^{3+} ions by κCG, followed by the formation of κCG-capped gold nanoparticles (AuNPs). As per literature, the reduction of Au^{3+} ions by κCG can proceed through multiple pathways. Initially, Au^{3+} ions become dispersed within the aqueous κCG matrix, forming a κCG–Au(III) complex (eqn (1)). This intermediate subsequently reacts with hydroxide ions, leading to the reduction of Au^{3+} to metallic gold and the generation of AuNPs capped by κCG chains (eqn (2)). In addition, the hydroxyl (–OH) and aldehyde (–CHO) groups present in κCG can play a significant role in electron donation, further assisting in the stepwise reduction of Au^{3+} ions to Au^0, accompanied by the oxidation of κCG functional groups (eqn (3) and (4)).[36]

$$Au^{3+}(aq) + \kappa CG(aq) \rightarrow [Au(\kappa CG)]^{+}(aq) \tag{1}$$

$$[Au(\kappa CG)]^{+} + OH^{-} \rightarrow 2Au(\kappa CG)\downarrow + H_2O + \tfrac{1}{2}O_2 \tag{2}$$

$$3(\kappa CG\text{–}CH_2OH) + 6OH^{-} + 2Au^{3+} - 6e^{-} \rightarrow 3(\kappa CG\text{–}CHO) + 6H_2O + 2Au^0 \tag{3}$$

$$3(\kappa CG\text{–}CHO) + 9OH^{-} + 2Au^{3+} - 6e^{-} \rightarrow 3(\kappa\text{-}CG\text{–}COO^{-}) + 6H_2O + 2Au^0 \tag{4}$$

For simplicity, we will use the following notations for different hydrogels:

Ink-A: 1.5% κCG hydrogel (blank).

Ink-B: 1.5% κCG hydrogel crosslinked with KCl salt.

Ink-C: 1.5% κCG hydrogel with *in situ* AuNPs (no salt).

Ink-D: 1.5% κCG hydrogel with *in situ* AuNPs (crosslinked with KCl salt).

The size of the *in situ* synthesized AuNPs was determined using dynamic light scattering (DLS), Fig. S1. For measurements, the hydrogel inks were first heated to 80 °C, diluted to a concentration of 1 mg ml^{-1} with deionized water, and subsequently cooled to room temperature prior to analysis. The number-weighted size distribution obtained under these conditions indicates a consistent hydrodynamic diameter of approximately 758 nm for both ink-C and ink-D. The relatively large size reflects the association of AuNPs with the κCG polymer matrix, stabilized through hydrogen bonding, van der Waals, and π–π interactions, confirming their uniform dispersion within the hydrogel network.[37]

Rheological characterization of hydrogel inks

The rheological properties of all the inks were evaluated 24 hours after preparation using a stress-controlled modular compact rheometer (Anton Paar MCR302). Rheological measurements for each ink were performed at 25 °C with a parallel plate geometry of 50 mm diameter (PP50) and a 0.5 mm gap between the measuring plate and the geometry. The samples were equilibrated for 10 minutes at 25 °C before performing the rheological tests. Before starting the flow curves measurement, all the inks were subjected to a low shear rate of

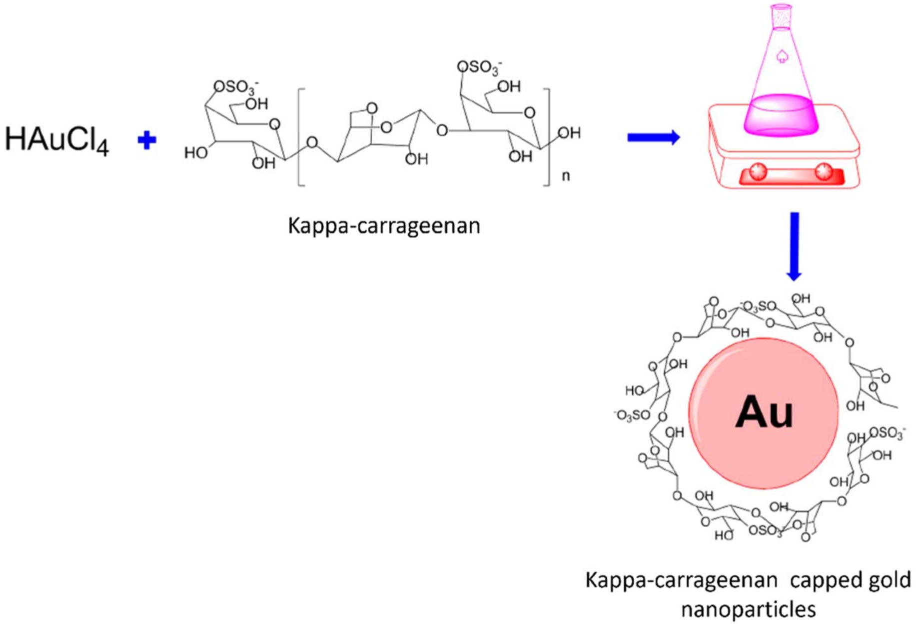

Fig. 1 Schematic diagram showing κCG reduced Au^{3+} ions and κCG capped gold nanoparticles (AuNPs).

0.01 s^{-1} for 300 seconds. Subsequently, flow curves were generated by logarithmically increasing the shear rate from 0.01 s^{-1} to 20 s^{-1} in order to evaluate the flow behavior of the hydrogel inks. The upper shear rate limit of 20 s^{-1} was selected to avoid experimental artifacts, as shear rates beyond this threshold resulted in noticeable sample slippage from the rheometer geometry. This issue was particularly evident in ink-B and ink-D, likely due to the increased crosslinking density imparted by the presence of KCl salt.

The non-Newtonian power law model was used to characterize their shear-thinning properties.[38] The Power Law model was chosen because it is simple yet effective in describing the key rheological features of shear-thinning fluids across a broad range of shear rates. The 'n' and 'K' values were calculated from the viscosity *versus* shear rate curves by fitting the non-Newtonian power law equation,[39] as shown in the eqn (5).

$$\eta = K\dot{\gamma}^{n-1} \tag{5}$$

where η is the ink's viscosity (Pa s), n is the flow behavior index (dimensionless), K is the flow consistency index (Pa s), and $\dot{\gamma}$ is the shear rate (s^{-1}). The value of K determines the initial viscosity of the hydrogel inks and ultimately provides a measure of the ink's extrudability.[40] If $0 < n < 1$, the fluid shows shear thinning or pseudo plastic behavior. Smaller is the value of n, greater is the degree of shear thinning. If $n = 1$, the fluid shows Newtonian behavior. If $n > 1$, the fluid shows shear thickening or dilatant behavior with a higher value of n resulting in great shear thickening.[34]

Oscillatory stress sweep measurements were conducted by logarithmically increasing the applied oscillatory stress from 0.1 to 100 Pa to evaluate the viscoelastic properties of the hydrogel inks. The test was performed in oscillatory mode at a constant angular frequency of 6.28 rad s^{-1}, using a PP50 geometry with a gap of 0.5 mm. All measurements were carried out at a constant temperature of 25 °C. The storage modulus (G') and loss modulus (G'') were recorded as a function of applied oscillatory stress. Apparent yield stresses were measured using oscillatory stress sweeps. The derivation of yield stress from such strain sweeps is debated. Although the crossover point of G' and G'' is often used as a benchmark, it typically occurs beyond the actual yield of the material and overestimates the apparent yield stress. A more reliable estimation was obtained by identifying the intersection of the tangents in the linear and nonlinear regions of G', providing values consistent with those from Herschel–Bulkley fitting.[41]

In addition, strain and frequency sweep tests were carried out using the same PP50 geometry. The linear viscoelastic region (LVR) was identified at 0.1% strain, which was then used for frequency sweep measurements. Strain sweeps were performed over the range of 0.001–1200% strain, while frequency sweeps were conducted from 0.1 to 100 rad s^{-1} to evaluate the dependence of viscoelastic moduli on strain and frequency.

X-ray diffraction (XRD)

XRD analysis was performed using a Rigaku SmartLab 9 kW diffractometer with Cu Kα radiation ($\lambda = 1.5406$ Å). Hydrogel inks were first frozen at −80 °C for 24 h, followed by lyophilization for 24 h. A thin film of the lyophilized sample (~0.1 mm) was prepared and placed on the sample holder for measurement. Diffractograms were recorded in the 2θ range of 5°–80°.

Fourier transform infrared (FTIR) spectroscopy

The functional groups present in the κ-carrageenan hydrogels were analyzed using a Bruker Invenio-S FTIR spectrometer.

Lyophilized samples were placed directly on the crystal stage and pressed with the ATR probe. Each sample was scanned over the spectral range of 400–4000 cm^{-1}.

Field emission scanning electron microscope (FESEM)

Field Emission Scanning Electron Microscope (FESEM) analysis was performed using a JSM-7600F (JEOL) microscope. Lyophilized samples of ink A, ink B, ink C, and ink D were used for imaging. Prior to analysis, the samples were sputter-coated with platinum for 120 s to ensure surface conductivity. The microstructure and surface morphology of the samples were studied under 50× magnification.

Thermal analysis

Thermal behavior of the four inks (A–D) was examined using a PerkinElmer TGA 4000 and DSC 8000. For TGA, lyophilized samples (5–10 mg) were heated from 25 to 700 °C at 10 °C min^{-1} under nitrogen to track weight loss and decomposition. For DSC, lyophilized samples (~5 mg) were heated from 25 to 300 °C at the same rate to capture transitions such as glass transition, helix-coil changes, and melting. These measurements were used to compare the stability of the inks, assess the influence of KCl and AuNPs on thermal properties, and relate thermal response to rheology and printability.

3D printing of hydrogel inks

All the hydrogel inks were prepared 24 hours prior to printing. The inks were then heated to 65 °C using a hot plate and poured directly into a 5 ml luer lock syringe. Measures were taken to avoid the inclusion of air bubbles during filling.[42] All the inks were printed using Allevi BioInk 3D printer, USA, equipped with a 23-gauge (23G) cylindrical nozzle, as shown in Fig. 2(a). To assess the printability of hydrogel inks, a single-layer grid design was printed, as shown in Fig. 2(b). Printing was performed at a constant temperature of 25 °C, with a constant print speed of 6 mm s^{-1}. The temperature of the printing bed was also kept constant at 25 °C. For analyzing the structural stability of the printed structures, the same design was printed without the internal grids in a multi-layer fashion with the same printing conditions.

To determine the printability of the hydrogel inks, the area and perimeter of the printed grid was measured. The printability was calculated using eqn (6).[43]

$$\mathrm{Pr} = \frac{L^2}{16\ A} \tag{6}$$

where, Pr is the printability of hydrogel ink, A is the area of the printed grid, and L is the perimeter of the printed grid.

CFD modeling

To better understand the 3D printing process using CFD modeling, the syringe–nozzle geometry that exactly represents the actual 3D printing setup was made using DesignModeler in ANSYS Fluent 2019 R1. To determine the dimensions of the syringe–nozzle geometry, as shown in Fig. 3(c), a vernier caliper was used, and internal dimensions were measured by performing image analysis using ImageJ software. The final geometry is shown in Fig. 3(a). For meshing of the geometry, a hexahedral mesh in ANSYS fluent was used, with the maximum target skewness of 0.9. The generated mesh has 3827 elements with 4853 nodes, as shown in Fig. 3(b).

CFD simulation

ANSYS fluent was used for steady-state simulations where all the hydrogel ink comprises the fluid domain, and it uses the finite volume method (FVM) for calculations. To simulate the extrusion process in ANSYS, the nozzle outlet was set to zero gauge pressure, representing the ambient atmospheric condition. For the inlet of the syringe, a constant mass flow rate of 1.67×10^{-6} kg s^{-1} was given, which was calculated by actual 3D printing experiments, corresponding to the print speed of 6 mm s^{-1}. The density of hydrogels was also measured, and was found to be 993.1 kg m^{-3}. For simulating the extrusion pressure, the non-Newtonian power law model with the shear rate dependent method was chosen in ANSYS fluent, and the values of n and K were obtained from the power law fitting of the flow curves

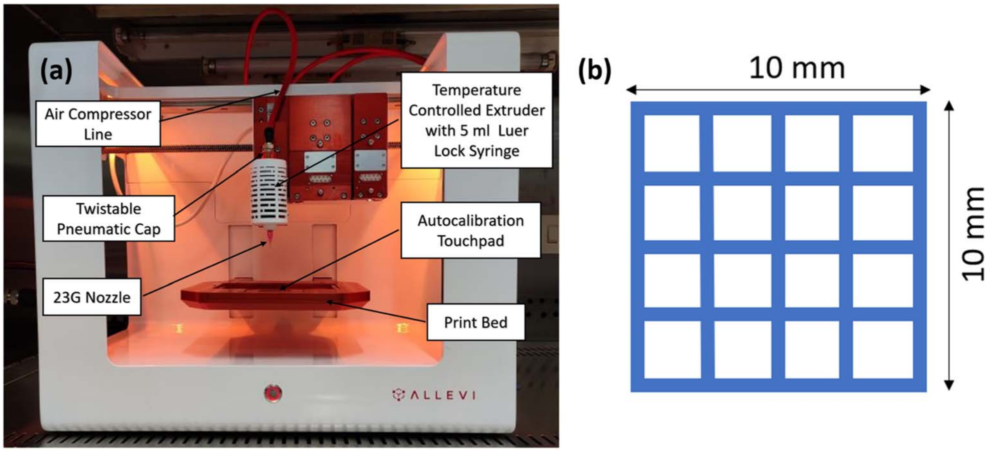

Fig. 2 (a) Allevi 3D bioprinter setup, and (b) CAD design for the 3D printed structures.

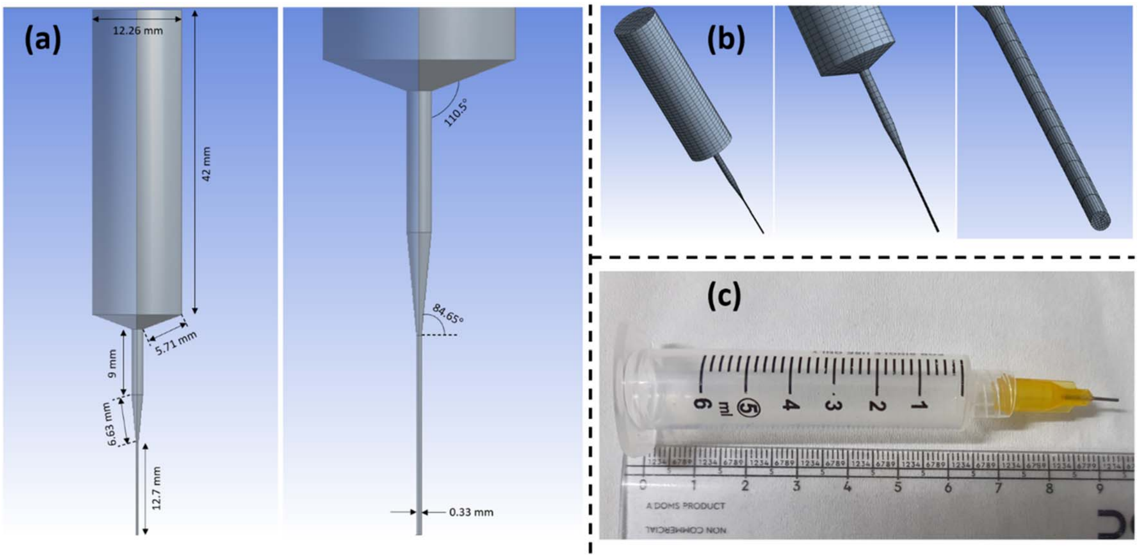

Fig. 3 (a) ANSYS-generated syringe–nozzle geometry, with cross-sectional view for various angles at different sections of the geometry. (b) Hexahedral meshing of the computational domain, highlighting the mesh structure in the syringe body and nozzle outlet. (c) Actual syringe with a 23G nozzle used for 3D printing experiments.

obtained from the rheology of hydrogels. The minimum and maximum viscosity values were also obtained directly from the flow curves for all the inks.

The coupled scheme was used for the pressure–velocity coupling. For the discretization of pressure, the Second Order method was used, while the Second Order Upwind method was used for the discretization of momentum. A mesh dependency analysis was also performed to ensure the reliability of the simulation results. To reduce the complexity of these CFD simulations, a few inherent assumptions were made. It was assumed that (a) the flow of all the hydrogel inks is incompressible, which means that the density remains constant at all points within the syringe; (b) the hydrogel flow during extrusion remains entirely within the laminar region; and (c) there was no slip between the hydrogel inks and all the walls of the syringe–nozzle geometry.

Establishment of flow models and assumptions

Since all the hydrogel inks follow non-Newtonian power law behavior shown by eqn (5). To simulate the extrusion process, the governing equations for the continuity as well as momentum conservation need to be solved.[44] For our simulations, we do not consider the energy equation, as the temperature is kept constant throughout the extrusion process.

Since the general continuity equation is:

$$\frac{\partial p}{\partial t} + \nabla\cdot(\rho\bar{v}) = 0$$

where p is the pressure, ρ is the density of hydrogel ink, $\bar{v}$ is the velocity vector, and t is the time. If the flow is incompressible (constant density), the continuity equation simplifies to:

$$\nabla\cdot\bar{v} = 0$$

The general equation for momentum conservation is:

$$\rho\left(\frac{\partial\bar{v}}{\partial t} + \bar{v}\cdot\nabla\bar{v}\right) = -\nabla p + \nabla\cdot\bar{\bar{\tau}} + F$$

where $\bar{\bar{\tau}}$ is the viscous stress tensor, and F is the body force per unit volume. In the case of gravity, $F = \rho g$. Since all the hydrogel inks have high viscosity and the extrusion nozzle is small, the effect of gravity can be neglected.[45] The momentum equation becomes:

$$\rho\left(\frac{\partial\bar{v}}{\partial t} + \bar{v}\cdot\nabla\bar{v}\right) = -\nabla p + \nabla\cdot\bar{\bar{\tau}}$$

The viscous stress tensor is defined by the following constitutive equation:[46]

$$\bar{\bar{\tau}} = 2\eta_{\text{eff}}D$$

where, η_{eff} is the effective viscosity (or non-Newtonian viscosity) of hydrogel inks, which is a function of shear rate $\dot{\gamma}$; and D is the rate of strain tensor or the deformation tensor, which is given by the following equation:

$$D = \frac{1}{2}\left(\nabla\bar{v} + (\nabla\bar{v})^{T}\right)$$

where, $\nabla\bar{v}$ is the velocity gradient while $(\nabla\bar{v})^{T}$ is the transpose of the velocity gradient. Other assumptions and boundary conditions are already mentioned in the previous section.

Thixotropy of hydrogel inks using CFD simulations

The thixotropy of all the hydrogel inks was measured by using the Anton Paar MCR302 rheometer after 24 hours of the sample preparation. Usually, the three-interval time thixotropy (3ITT) experiments were performed, which measures the viscosity at three shear intervals as a function of time. This helps to analyze how much of the initial viscosity can be recovered and the time required for the same.[47] Since we are concerned about the deformation of hydrogel inks during extrusion printing, there is no such method to find the shear rates that act upon the ink during printing. Hence, we are using the CFD simulations to predict the shear rates that exist during the 3D printing, and based on the results, we have made a new protocol to determine the thixotropy of hydrogels. In this protocol, we first apply a low shear rate of 0.01 s^{-1} for 300 s, which represents the shear rates within wall-1 as shown in Fig. 4. Then, we increase the shear rates to 5 s^{-1} for 90 s, which represents the flow through wall-3 (Fig. 4). Then, the shear rate is finally increased to 500 s^{-1} for 90 s, representing the flow through the wall-5 (nozzle, Fig. 4). Now, as the ink is extruded out of the nozzle, a low shear rate of 0.01 s^{-1} is applied for 90 s. The extent of viscosity recovery is measured by comparing the plateau viscosities at a final low shear rate of 0.01 s^{-1} to the initial viscosity in wall-1. In addition to the degree of viscosity recovery, the kinetics, or time scales involved, are significant indicators of print fidelity. Agarwal *et al.* demonstrated that the recovery of storage modulus after applying a large amplitude oscillatory shear can be divided into three distinct phases: (1) a steep increase in storage modulus, (2) a slower increase in storage modulus, and (3) a plateau in storage modulus.[48] The authors found that improved printing fidelity is associated with formulations that exhibit a faster or shorter time scale of increase in storage modulus during the first phase. Consequently, the quicker the viscosity recovers as the ink is extruded from wall-5 to the printing bed, the better the printing outcome will be.

Since wall-2 and wall-4 are the converging zones that connects wall-1 to wall-3 and wall-3 to wall-5, the shear rates within these regions also vary between the shear rates of the walls it connects, as shown in Fig. 4. Therefore, the effect of these converging walls was neglected while making the thixotropy protocol.

Results & discussion

Rheology of hydrogel inks

To understand how shear rate affects the viscosity of the hydrogel inks and to evaluate their printability, it is highly important to study their rheological properties. The change in viscosity with varying the shear rates from 0.01 s^{-1} to 20 s^{-1} is observed with the help of flow curves, as shown in Fig. 5(a)–(d). It can be seen from the flow curves that the viscosity of all the hydrogel inks decreases with increasing shear rates, which shows that all the inks have "shear thinning" behavior. This is because of the disentanglement of polymeric networks within the hydrogel structure due to the application of shear rate. When this rate of disentanglement becomes greater than the network reconstruction rate, the hydrogels show a decrease in viscosity, depicting the shear thinning behavior.[49]

Since all the hydrogel inks exhibit shear thinning behavior, and their viscosity decreases almost linearly on a log–log plot, the non-Newtonian power law model, as shown in eqn (5), is typically used to fit the flow curves. All the flow curves were fitted using the non-Newtonian power law model in ORIGIN software, and the fitting parameters n and K, along with their corresponding R^2 values, are reported in Table 1. These values

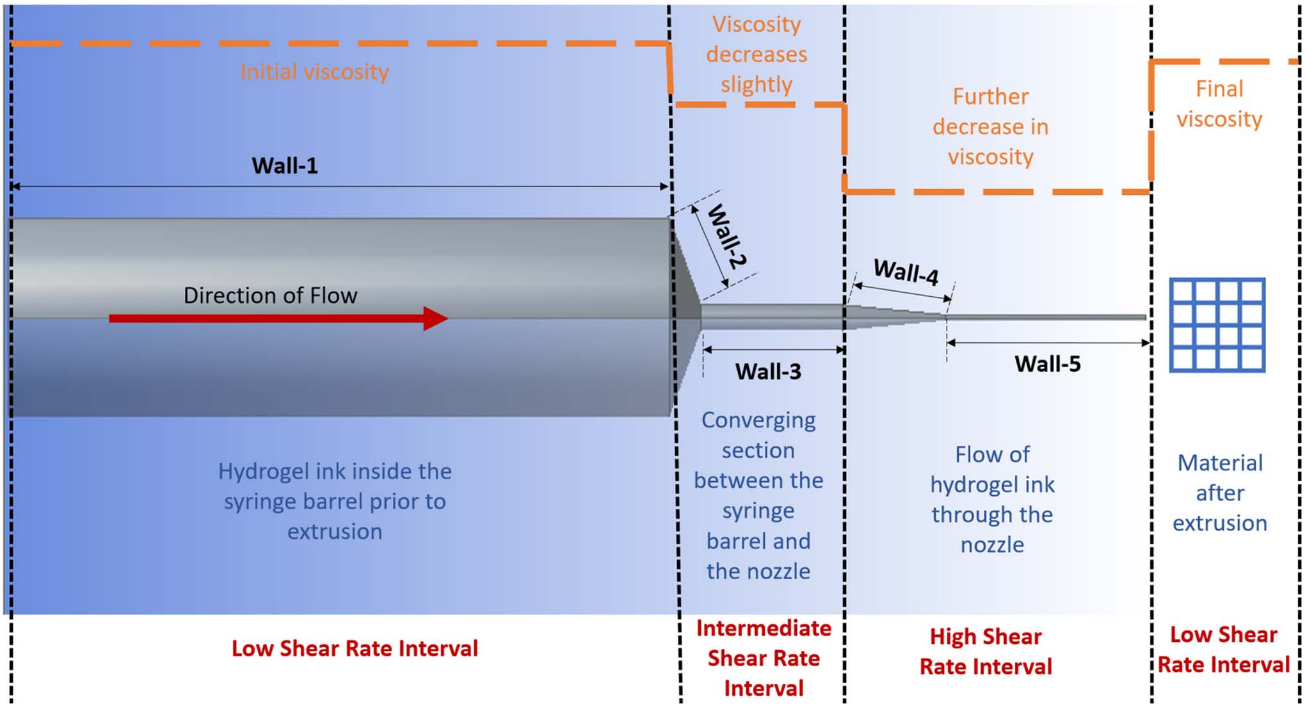

Fig. 4 Schematic representation of shear rate and viscosity variation at different locations within the syringe–nozzle geometry.

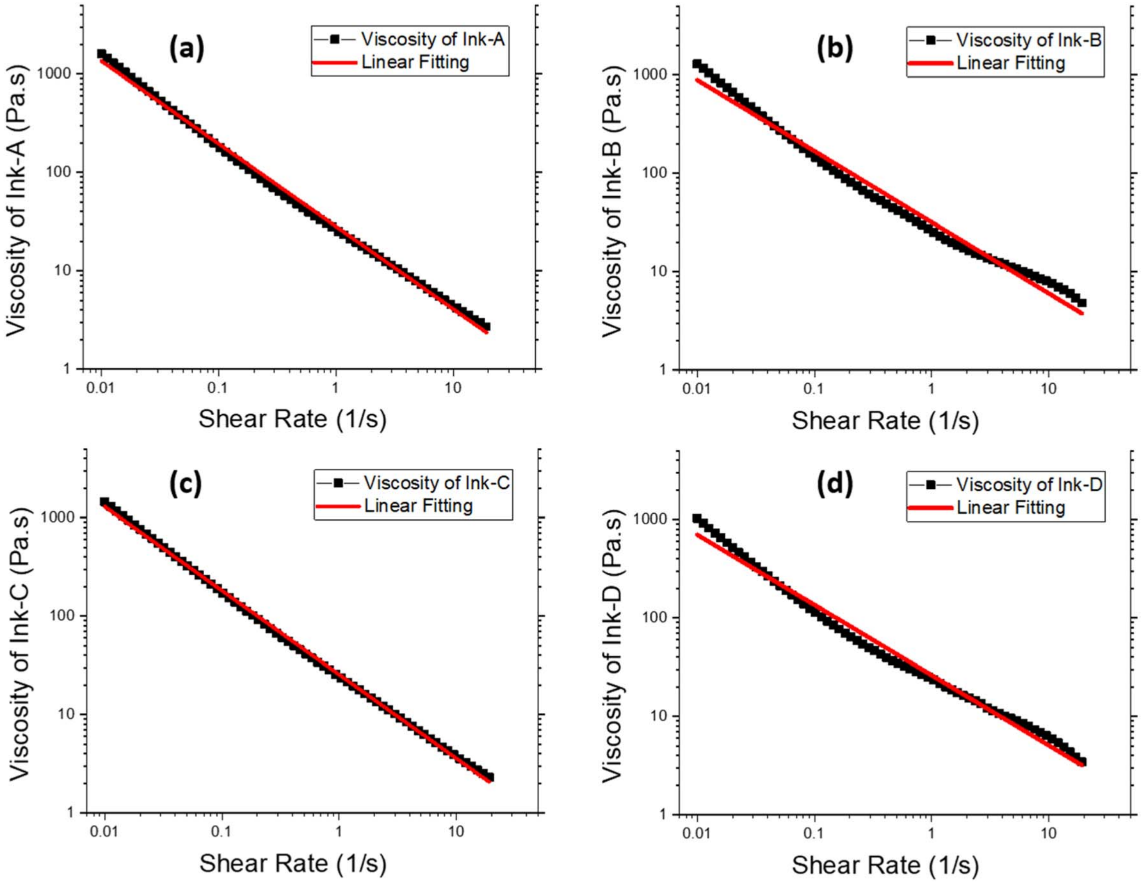

Fig. 5 Flow curves with shear rates varying logarithmically from 0.01 s^{-1} to 20 s^{-1} for (a) ink-A, (b) ink-B, (c) ink-C, and (d) ink-D.

Table 1 Coefficients from non-Newtonian power law model fitting

Serial number	Hydrogel ink	n	K	R^2
1	Ink-A	0.159	28.25	0.9978
2	Ink-B	0.279	32.0	0.9854
3	Ink-C	0.147	25.5	0.9991
4	Ink-D	0.286	26.23	0.9884

were then used to represent the non-Newtonian behavior of the hydrogel inks in CFD simulations performed in ANSYS Fluent.

As shown in Fig. 6(b), the strain sweep results indicate that ink-A and ink-C exhibit a larger linear viscoelastic region (LVR) compared to ink-B and ink-D, likely due to their less crosslinked structure, which allows the polymer chains to deform more before network disruption. In contrast, ink-B and ink-D show higher G' values, with ink-B at 652.4 Pa and ink-D at 534.3 Pa, whereas ink-A and ink-C exhibit lower G' values of 224.3 Pa and 204.1 Pa, respectively. The higher G' in ink-B and ink-D is attributed to the presence of KCl, which promotes physical crosslinking within the hydrogel network, increasing stiffness and mechanical stability[24] while reducing the extent of the LVR. Apparent yield stresses of the hydrogel inks were determined from oscillatory stress sweeps, using the intersection of tangents in the linear and nonlinear regions of G' (Fig. 6(a)), which provides a more accurate estimation compared to the conventional G'–G'' crossover method.[50] All hydrogel formulations exhibited well-defined yield stress behavior, with values ranging from 13 to 20 Pa. These results indicate that the inks possess sufficient structural integrity to maintain their shape after deposition, confirming their suitability for extrusion-based 3D printing applications.

FTIR analysis

The FTIR spectra of lyophilized κ-carrageenan-based inks (A–D) exhibited characteristic absorption peaks with subtle variations depending on formulation (Fig. 7). Inks A and B displayed a broad O–H stretching band centered at 3372 cm^{-1}, whereas in inks C and D this band was shifted to 3355 cm^{-1}.[51] This shift of the bonded O–H stretching in the presence of AuNPs indicates the participation of hydroxyl groups in the reduction of Au^{3+} cations and subsequent capping of AuNPs within the κCG matrix.[36] The width of this band followed the order ink D > ink C > ink A > ink B, indicating stronger intermolecular interactions in ink D (κCG + AuNPs + KCl), likely due to the combined effect of AuNP–κCG interactions and ionic crosslinking. Ink C (κCG + AuNPs) also showed broader bands than ink A (pure κCG), consistent with interactions between AuNPs and the κCG matrix, while ink B (κCG + KCl) exhibited the narrowest band,

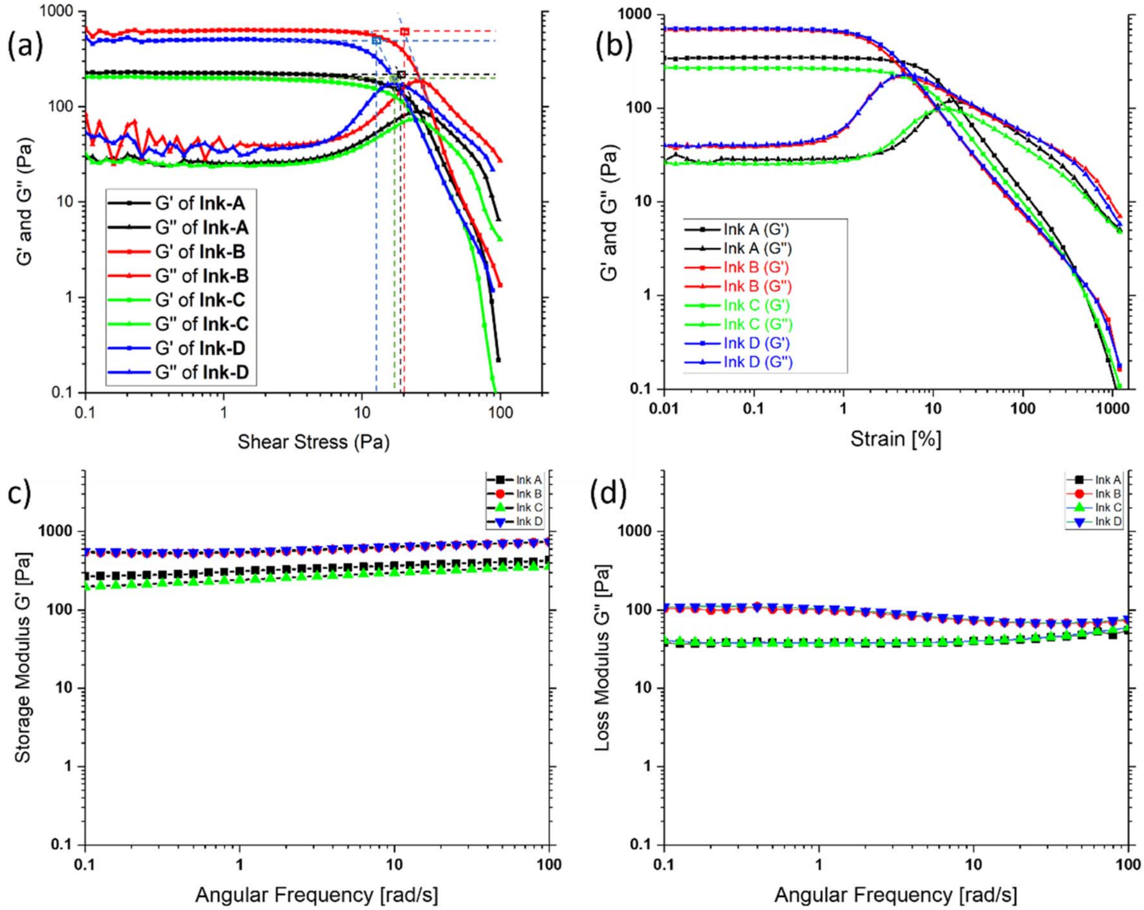

Fig. 6 Rheological characterization of κ-carrageenan-based hydrogel inks (A–D). (a) Storage modulus (*G*′) and loss modulus (*G*″) as a function of shear stress (oscillatory stress sweep). (b) *G*′ and *G*″ as a function of strain (strain sweep) to determine the linear viscoelastic region (LVR). (c) *G*′ *versus* angular frequency and (d) *G*″ *versus* angular frequency (frequency sweep).

suggesting reduced bound water mobility due to KCl-mediated stabilization. A secondary band corresponding to C–H stretching appeared at 2918 cm^{-1} in inks A and D, while it was slightly shifted to 2914 cm^{-1} in inks B and C.[36]

Additional peaks were observed at 1635 cm^{-1} corresponds to vibrations of bound water,[51,52] whereas the band at 1228 cm^{-1} is attributed to asymmetric S=O stretching of sulfate groups.[52] The signals at 1035, 920 and 842 cm^{-1} arise from the glycosidic linkage, C–O–C stretching of 3,6-anhydro-D-galactose and the O–S–O symmetric vibration of sulfate esters, respectively, which are characteristic features of κCG.[51,52]

These spectral features confirm the retention of the primary κCG structure across all formulations while highlighting spectral shifts due to AuNP incorporation and KCl crosslinking. In particular, the O–H band broadening and shift in inks C and D reflect enhanced κCG–AuNP interactions and stronger network stabilization.

XRD analysis

The XRD patterns (Fig. 8) of the hydrogel inks reveal predominant amorphous characteristics with variations depending on composition. Ink-A shows a broad halo between 15°–25° 2*θ*, characteristic of the amorphous κCG matrix. Ink-B, while retaining the amorphous halo, exhibits reduced intensity, indicating that KCl addition lowers the overall amorphous content. Ink-C maintains the amorphous halo but also displays a sharp peak at 44.5°, corresponding to the (200) reflection of face-centered cubic gold, confirming the presence of crystalline AuNPs. In ink-D, this sharp Au peak disappears upon KCl addition, suggesting strong dispersion of AuNPs and suppression of detectable crystallinity. Furthermore, similar to ink-B, ink-D also shows reduced amorphous halo intensity compared to ink-A and ink-C. Overall, the XRD results confirm the predominantly amorphous nature of κCG -based inks, with salt incorporation diminishing amorphous halo intensity and influencing the detectability of AuNP crystallinity.

FESEM analysis

FESEM imaging (Fig. 9) of lyophilized κCG -based inks (A–D) revealed a porous and wrinkled surface morphology across all formulations. Among the samples, ink-A exhibited the highest density of pores, indicating a more open structure whereas ink-D showed comparatively a smaller pore count, demonstrating a denser configuration. Inks B and C displayed intermediate

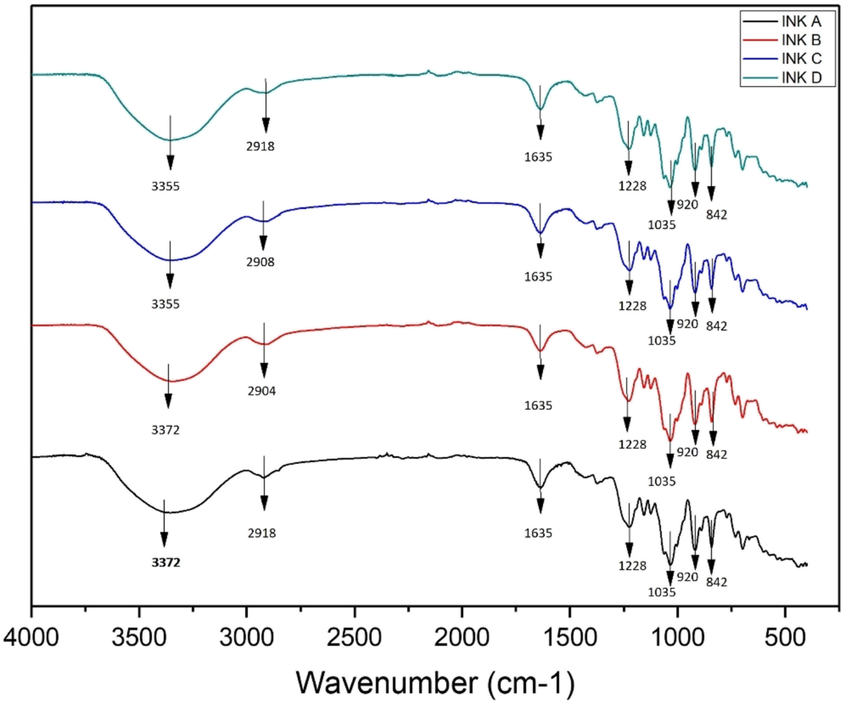

Fig. 7 FTIR spectra of lyophilized κ-carrageenan-based hydrogel inks (A–D).

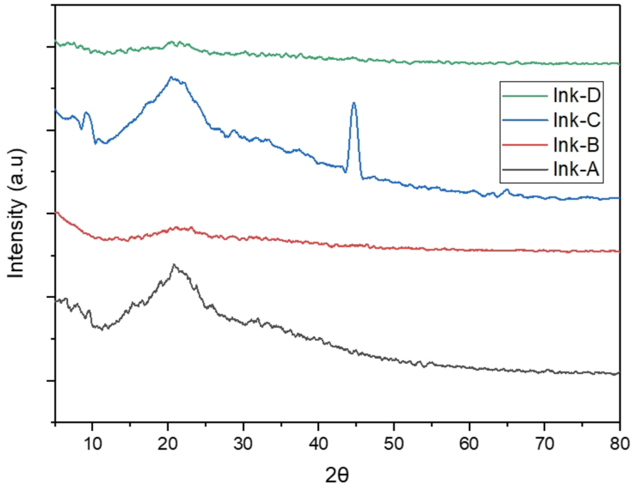

Fig. 8 XRD patterns of κ-carrageenan-based hydrogel inks (A–D).

morphologies, confirming that both AuNP incorporation and KCl crosslinking influence the pore structure in the hydrogels. Overall, the observations indicate that formulation composition modulates the pore density of κCG -based inks, which may directly impact their mechanical stability and printability.

Thermal analysis

The thermal degradation profiles (Fig. 10(a)) of the four inks showed distinct differences depending on the presence of KCl and AuNPs. All samples exhibited an initial mass loss below 110 °C, corresponding to evaporation of bound water,[53] with ink A showing the highest weight loss in this region. The main decomposition stage occurred between 225–253 °C. Inks containing AuNPs (C and D) degraded earlier (onset 228–229 °C) compared to AuNP-free inks (A and B, onset 235–240 °C). Quantitatively, ink C lost 12 wt% (from 89 wt% to 77 wt%), ink B lost 13 wt% (86 wt% to 73 wt%), ink D lost 13 wt% (87 wt% to 74 wt%), and ink A lost 18 wt% (82 wt% to 64 wt%) within the 228–253 °C range.

At later stages, beyond 460 °C, ink B exhibited a pronounced additional weight loss, which can be attributed to KCl-related effects that promote further matrix destabilization. Interestingly, this secondary degradation was not observed in ink D, indicating that the presence of AuNPs altered the decomposition pathway. The presence of AuNPs likely shifted the breakdown of organic matter to earlier stages, leaving minimal material for decomposition at higher temperatures. Overall, inks containing AuNPs degraded at lower onset temperatures but showed more stabilized profiles at higher temperatures compared to κCG-KCl-only inks.

The DSC thermograms (Fig. 10(b)) of inks A–D exhibited single major endothermic transitions at 249 °C (ink A), 248 °C (ink B), 242 °C (ink C), and 239 °C (ink D). These peaks correspond to the disruption of polymer–polymer and polymer–ion interactions within the κCG hydrogel matrix. The slight decrease in transition temperature upon AuNP incorporation (inks C and D) perhaps indicates reduced chain entanglement and weaker hydrogen bonding, which aligns with the lower thermal stability observed in TGA results. The small shift between ink A and KCl-crosslinked ink B suggests that ionic interactions stabilize the matrix but do not significantly alter its thermal response.

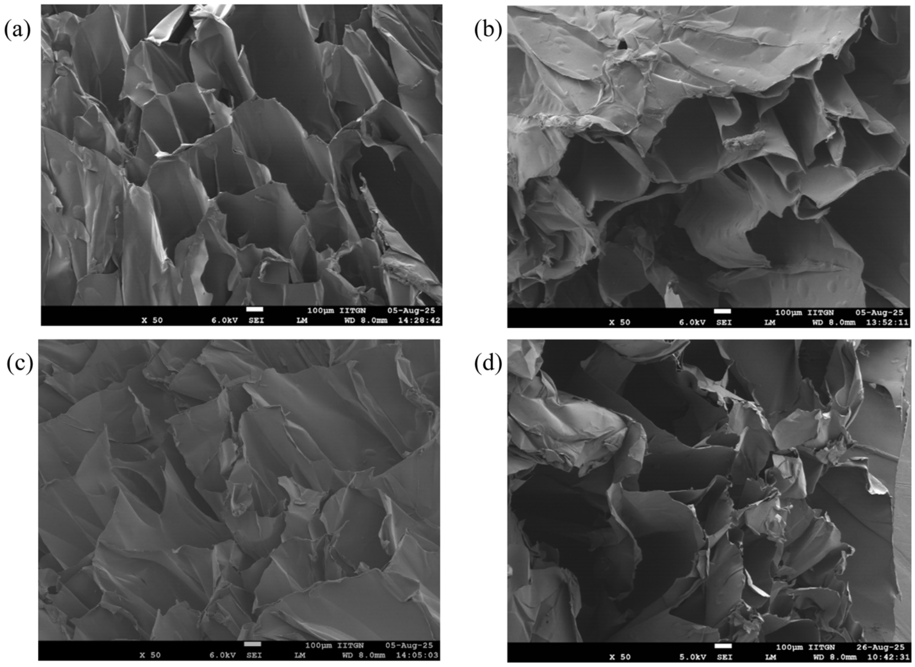

Fig. 9 FESEM images of κ-carrageenan-based hydrogel inks (A–D). Images show the microstructural morphology of (a) ink A, (b) ink B, (c) ink C, and (d) ink D.

3D printing of hydrogel inks

Single-layer printing. In order to evaluate the printability of the hydrogel inks, a simple square structure measuring 1 cm in length with internal grids was printed, and the printing results are shown in Fig. 11. The printing results of ink-A at different printing pressures, ranging from 5 to 7 psi (=34.5 to 48.3 kPa), and at a constant temperature of 25 °C are shown in Fig. 11(a). We can clearly see that at the extrusion pressure of 5 psi (=34.5 kPa), the ink is not extruded properly, and hence, the internal grids cannot be printed due to the lower extrusion pressure. At 6 psi (=41.4 kPa), the ink is extruded properly out of the nozzle, and the desired structure is printed, having a fine outline and internal grids. However, when the extrusion pressure was further increased to 7 psi (=48.3 kPa), over-extrusion occurred. This led to bulkier printed grids that expanded before gelation, ultimately causing the entire structure to collapse and lose its intended fine-grid morphology. Here, we can say that 6 psi (=41.4 kPa) is the optimum pressure for the extrusion of ink-A.

For ink-B, the printing results are shown in Fig. 11(b). We can observe that the extrusion pressures required for ink-B are significantly higher than that of ink-A. The optimal extrusion pressure for ink-B was found to be 17 psi (=117.2 kPa). We believe this is because in ink-B, the κCG molecules are dissolved in 10 mM KCl salt solution, which promotes aggregation of the helices from different κCG domains. These aggregated helices undergo cross-linking, leading to the formation of a cohesive network.[54] As a result, the hydrogel ink exhibits improved

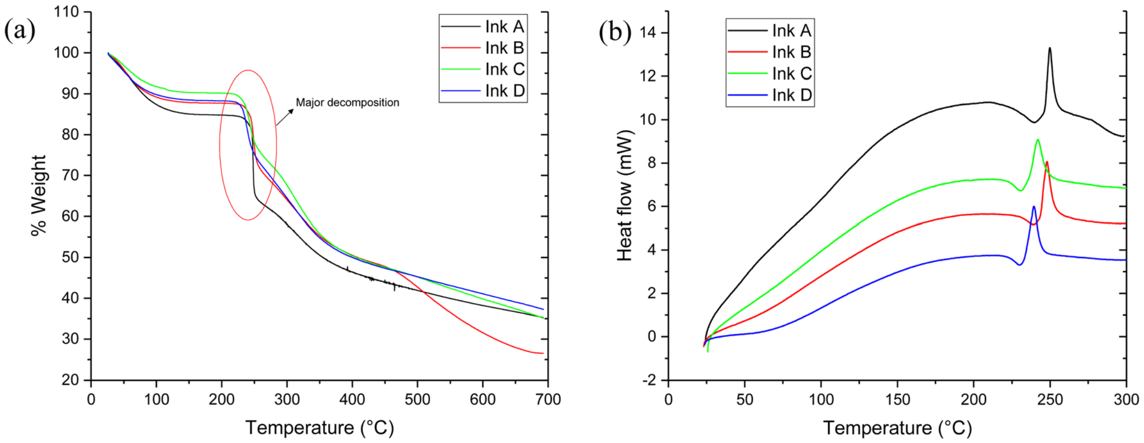

Fig. 10 Thermal analysis of κCG-based hydrogel inks (A–D): (a) TGA curves and (b) DSC thermograms.

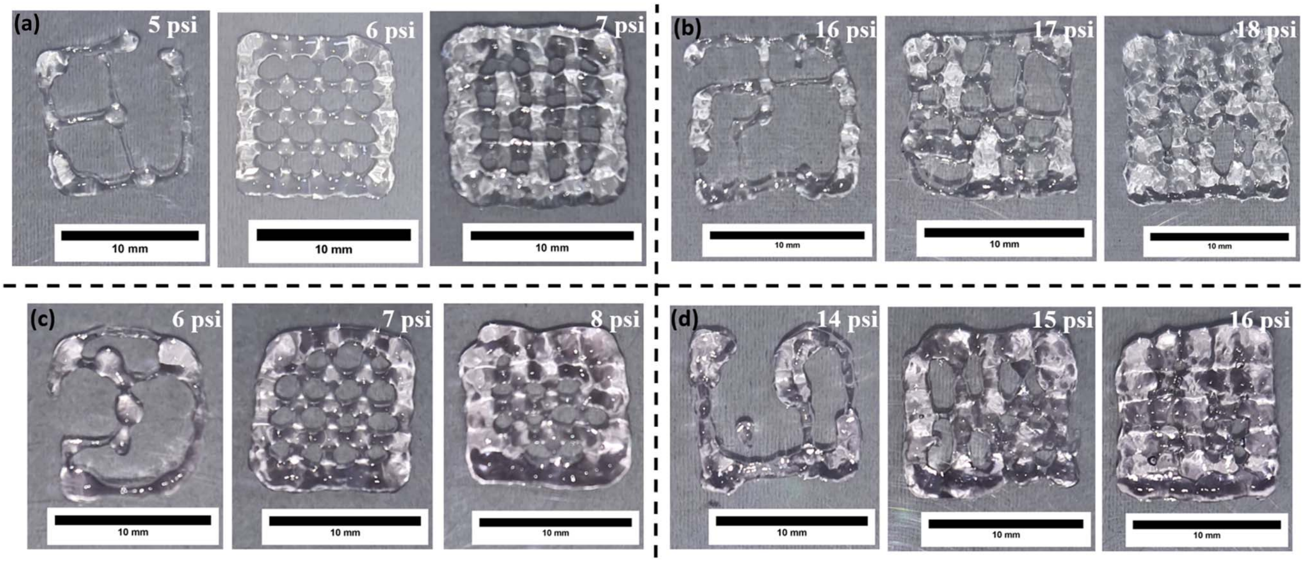

Fig. 11 Printing results at different pressures for (a) ink-A, (b) ink-B, (c) ink-C, (d) ink-D. Temperature is kept constant at 25 °C.

mechanical strength also reflected in a higher G' value (Fig. 6(a)); however, its ability to produce well-defined printed structures is diminished.

For ink-C, the extrusion pressures are close to those of ink-A, with an optimum printing pressure of 7 psi (=48.3 kPa), as shown in Fig. 11(c). Although ink-C has AuNPs incorporated into its structure, these nanoparticles do not alter the κCG hydrogel network but may slightly increase the overall stiffness of the structure.[55] Due to this, there is a slight increase in the optimum printing pressure of ink-C compared to that of ink-A. For ink-D, the extrusion pressures are high and comparable to those of ink-B, as both inks have hydrogel network structures cross-linked by the addition of KCl salt, resulting in higher G' values (Fig. 6(a)). Ink-D also contains *in situ* synthesized AuNPs, which contribute to improved shear-thinning behavior.[56] Due to the enhanced shear-thinning property as indicated by, ink-D requires slightly lower extrusion pressures than ink-B, with an optimum printing pressure of 15 psi (=103.4 kPa), as shown in Fig. 11(d).

To quantitatively analyze the printability of the hydrogel inks, eqn (6) was used for the calculations. The analysis was performed on three different printed structures at the optimum pressure for each hydrogel ink, as shown in Fig. S2 in SI. ImageJ software was used to extract the values of L and A for all the internal grids. The final printability values, averaged over the three measurements, are reported in Table 2. The results indicate that ink-A has the highest printability, primarily due to its soft polymeric network, which facilitates smooth extrusion through the narrow nozzle and enables the formation of well-defined structures with minimal resistance.[24] Ink-C also exhibits good printability, albeit slightly lower than ink-A. This reduction is attributed to the incorporation of AuNPs within the hydrogel network, which slightly increases the stiffness of the ink and consequently hinders the extrusion performance. However, ink-B and ink-D exhibit very low printability compared to the other two hydrogel inks. This is primarily because the presence of KCl salt promotes crosslinking within the hydrogel matrix, which ultimately increases the ink's mechanical strength and also enhances the gelation properties.[54] Hence, these inks have a greater tendency to clog at the nozzle outlet, ultimately creating an obstruction in smooth extrusion and resulting in decreased printability.

Table 2 Printability values for different hydrogel inks

Serial number	Hydrogel ink	Printability values
1	Ink-A	0.88
2	Ink-B	0.65
3	Ink-C	0.83
4	Ink-D	0.46

Multi-layer printing. To analyze the mechanical strength and structural stability of the hydrogel inks, each ink was printed in multiple layers, up to a total of 20 layers. Printing was carried out using the respective optimum conditions for each ink, and the results are shown in Fig. 12(a)–(d). To assess structural stability, the printed samples were kept under ambient conditions and imaged again 30 minutes after printing.

From the results, it can be seen that ink-A was unable to print a well-defined structure. The printed walls were uneven and began to sag shortly after deposition, which caused the structure to become broader at the base. This shows that the ink does not have enough mechanical strength and structural integrity to support vertical stacking during multi-layer printing.[24] Once printed, the structure was kept in ambient conditions for 30 minutes. During this time, it could not support its own weight and eventually collapsed due to gravity. This clearly shows the poor structural stability of ink-A during multi-layer printing.

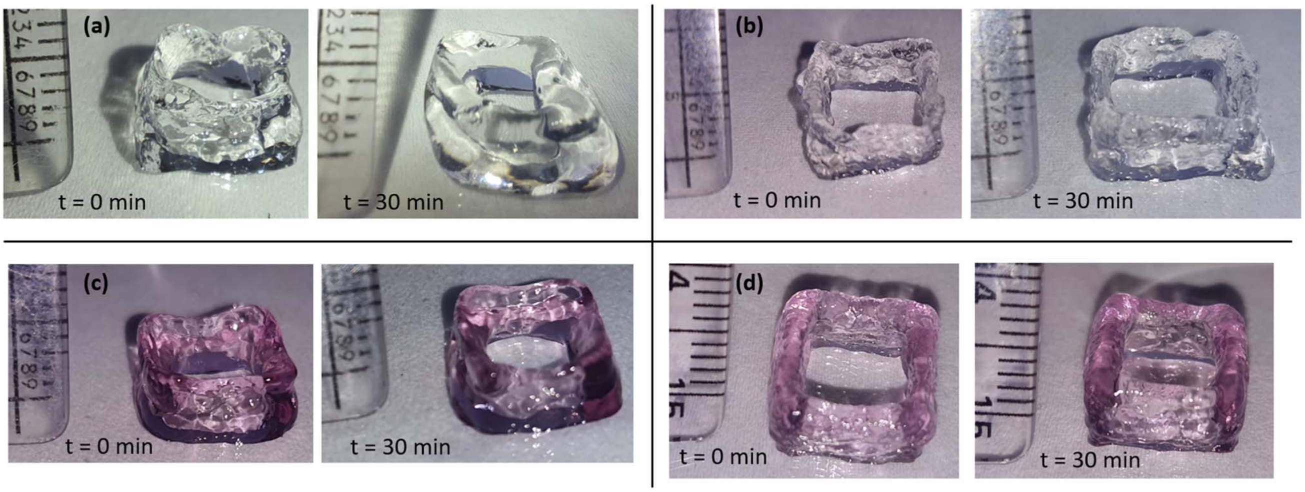

Fig. 12 Multi-layer printing (20 layers) results at $t = 0$ and $t = 30$ minutes of (a) ink-A at 6 psi, (b) ink-B at 17 psi (c) ink-C at 7 psi (d) ink-D at 15 psi. Temperature is kept constant at 25 °C.

During the multi-layer printing of ink-B, the extrusion behavior was inconsistent. Due to the cross-linking of the hydrogel with KCl salt, partial clogging occurred within the nozzle, which disrupted the flow of the hydrogel ink during extrusion.[54] In some regions, the extrusion was proper; however, the overall flow remained uneven, with intermittent interruptions and reduced extrusion in certain areas. As a result, the final height of the printed structure was lower than expected. Despite these extrusion issues, the structure exhibited good mechanical stability because of its high G' value, and no sagging was observed even after 30 minutes under ambient conditions. Ink-C was extruded properly under its respective optimum printing conditions. Compared to ink-A, it contains *in situ* synthesized AuNPs, which may contribute to increased stiffness in the printed structure.[55] Although the printed walls appeared slightly uneven, the presence of AuNPs provided the mechanical strength needed to support the multilayer structure, with only minimal broadening observed at the base. After being kept in ambient conditions for 30 minutes, the structure remained intact and successfully retained its structural integrity.

For ink-D, the multi-layer structure was well printed, with evenly printed walls and no sagging was observed at the base of the structure. Since ink-D was crosslinked with KCl, it exhibits a high G' value, providing sufficient mechanical strength to support the multi-layer structure. Additionally, the *in situ* synthesis of AuNPs enhanced the shear-thinning behavior of the hydrogel ink.[56] Together, these features provided the necessary physical properties for smooth extrusion and stable multi-layer printing. The printed structure remained highly stable and showed no signs of sagging, even after being kept for 30 minutes under ambient conditions.

Ink-D was also printed up to 50 layers under the same optimum conditions, and the structure was examined for any signs of collapse or deformation. As can be seen in Fig. 13, the printed structure remained stable up to 50 layers, with well-defined walls and no noticeable broadening at the base. After being kept for 30 minutes under ambient conditions, the structure showed no signs of sagging and retained its shape, demonstrating excellent multi-layer printability and strong structure retention ability.

Since ink-A exhibited the highest printability in single-layer printing and ink-D performed best in multi-layer constructs, these two inks were further evaluated using complex CAD designs, as shown in SI. In all printed designs, ink-A produced finer features compared to ink-D, attributed to the broader strand width observed with ink-D. As shown in Fig. S4, a five-layer structure printed with ink-A had a narrower width than a single-layer structure printed with ink-D. This is likely due to the higher extrusion pressure required for ink-D, resulting in higher material extrusion. Consequently, ink-D showed lower printability for designs with fine grids, as the increased strand width caused adjacent lines to merge, reducing print fidelity (Fig. 11(a)). However, for structures without fine features, ink-D remains a viable option due to its superior structural stability.

CFD simulations using ANSYS

CFD simulations were carried out for all the hydrogel inks; however, parameter profiles are presented here only for ink-A.

Simulated pressure profile. As shown in Fig. 14(a) and (b), the pressure profile for ink-A demonstrates a continuous

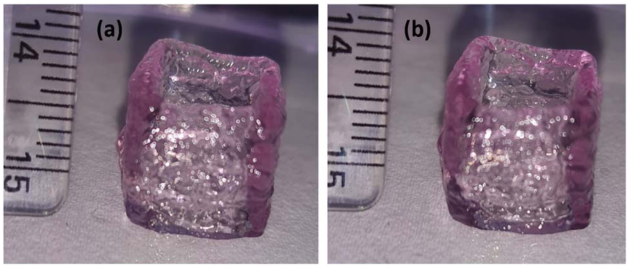

Fig. 13 Multi-layer printing (50 layers) results at 15 psi for ink-D at (a) $t = 0$, and (b) $t = 30$ minutes.

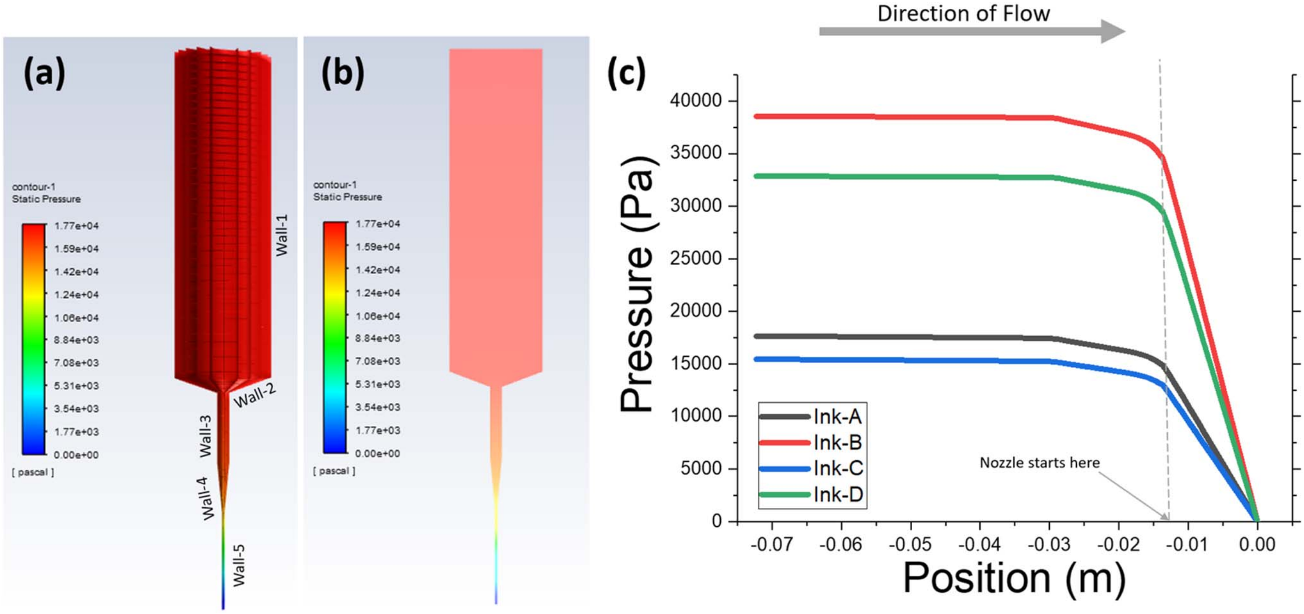

Fig. 14 (a) Pressure profile generated using ANSYS fluent for ink-A. (b) 2D representation of the pressure profile. (c) Pressure *vs.* position plot for all the hydrogel inks, generated using CFD simulations in ANSYS fluent.

decrease in the pressure along the length of the geometry, with the maximum gauge pressure of 17.7 kPa (=2.57 psi) observed at the syringe inlet, gradually reducing to zero gauge pressure at the nozzle outlet. A major drop in pressure was observed within the nozzle region, consistent with the findings reported by Guo *et al.* (2021) and Nikolaou *et al.* (2025).[57,58] This maximum pressure at the syringe inlet is the predicted value obtained from the CFD simulations, indicating the pressure required for proper extrusion of ink-A at a constant temperature of 25 °C.

Upon comparing the predicted pressure of 2.57 psi with the actual extrusion pressure of 6 psi used during the 3D printing experiments, it can be observed that the simulated values are lower than the experimental ones. This difference mainly arises due to the assumptions made while performing the CFD simulations. The CFD model does not account for factors such as friction between the hydrogel and the walls of syringe–nozzle geometry, interactions between successive layers of the hydrogel ink, or the influence of AuNPs and their potential interactions with the hydrogel as well as with other nanoparticles. These assumptions help to simplify the model and make the complex calculations easier, faster, and computationally less expensive. Although the model simplifies the system and predicts the pressure values lower than the actual pressures, it also shows consistent results with similar deviations from the predicted pressures required for all the hydrogel inks. In all the results, as shown in Table 3, the actual pressures are approximately 2.5 to 3 times the predicted pressures. Such a direct comparison between the predicted and actual extrusion pressures is not commonly found in the literature. It is likely because it is challenging to account for all the relevant interactions, making accurate pressure prediction more difficult. However, this study provides a reasonably good estimation of the extrusion pressures for all the hydrogel inks using only their rheological properties, and that too at a very low computational cost. As far as these predictions are concerned, they serve as a good starting point for conducting the extrusion tests, which can then be fine-tuned to determine the optimum printing pressures.

Fig. 14(c) shows the pressure *versus* position plots along the central axis of the syringe–nozzle geometry for all the hydrogel inks. The pressure required for the extrusion of ink-A and ink-C is significantly lower compared to that of ink-B and ink-D. This increase in pressure for ink-B and ink-D can be correlated to the enhanced crosslinking induced by the addition of KCl salt. Furthermore, the plots indicate that pressure variation along the syringe barrel is minimal, with the majority of the pressure drop occurring in the nozzle region, where the ink undergoes the most constriction.

Simulated velocity profile. Since the mass flow rate was determined experimentally for each hydrogel ink and the same value was used as the inlet boundary condition in the CFD simulations, the resulting velocity profiles remain nearly identical across all the hydrogel inks. This is primarily because of the assumption of incompressible flow, which causes the density to remain constant throughout. Given that velocity is directly related to the mass flow rate and inversely related to the cross-sectional area and fluid density, as represented in eqn (7), this consistency in the velocity profile is expected. Hence, the velocity field does not offer any distinct variation between the inks under the given conditions.

$$\text{Velocity} = \frac{\text{mass flowrate}}{\text{area} \times \text{density}} \tag{7}$$

For all the hydrogel inks, the velocity profile appears to remain within the laminar flow regime, as shown in Fig. 15.

Table 3 Predicted pressures using CFD simulations and the actual 3D printing pressures for all the hydrogel inks

Serial number	Hydrogel ink	Predicted extrusion pressure (kPa)	Experimental extrusion pressure (kPa)
1	Ink-A	17.7 (=2.57 psi)	41.4 (=6 psi)
2	Ink-B	38.6 (=5.60 psi)	117.2 (=17 psi)
3	Ink-C	15.5 (=2.24 psi)	48.3 (=7 psi)
4	Ink-D	32.9 (=4.77 psi)	103.4 (=15 psi)

Consistent with the observations of Nikolaou *et al.* (2025) and Oyinloye *et al.* (2022), the simulation results indicate that the majority of velocity development occurs within the cylindrical region of the nozzle, where the flow adopts the characteristics of a fully developed laminar profile, as illustrated in Fig. 15(b).[44,58] The maximum velocity obtained from the simulations is 28 mm s^{-1} for all the hydrogel inks, which corresponds to the peak velocity at the nozzle exit. Since the flow is laminar, and it is known that in such cases, the average velocity is half of the maximum velocity, the average extrusion velocity can be estimated to be around 14 mm s^{-1}.

Ideally, for consistent extrusion during 3D printing, the velocity of the print head should match the velocity of the extruded material, resulting in printed strand widths equal to the nozzle outlet diameter. In this study, the print head moves at a constant velocity of 6 mm s^{-1} with a nozzle diameter of 0.33 mm. However, the width of the extruded material is greater than the nozzle diameter, indicating that more material is being extruded compared to the ideal case. This suggests that the actual extrusion velocity is higher than 6 mm s^{-1}. Therefore, the simulated extrusion velocity of approximately 14 mm s^{-1} provides a reasonable and realistic estimate of the true extrusion behavior.

From the velocity *versus* position plots along the central axis of the syringe–nozzle geometry for all the hydrogel inks, as shown in Fig. 15(d), it is evident that despite significant variation in the printing pressures required for different inks, the velocity profiles remain largely unaffected. This is because of the imposed boundary condition of a constant mass flow rate at the inlet. The plots also reveal that velocity development primarily occurs as the hydrogel approaches the nozzle entrance, reaching a maximum at the central axis, and remains constant thereafter until extrusion is complete.

Simulated viscosity profile. Fig. 16(a) and (b) shows the viscosity profile of ink-A, highlighting how the viscosity varies across different regions of the geometry due to spatial differences in shear stress. These shear stresses primarily arise near the walls, where the no-slip boundary condition holds the

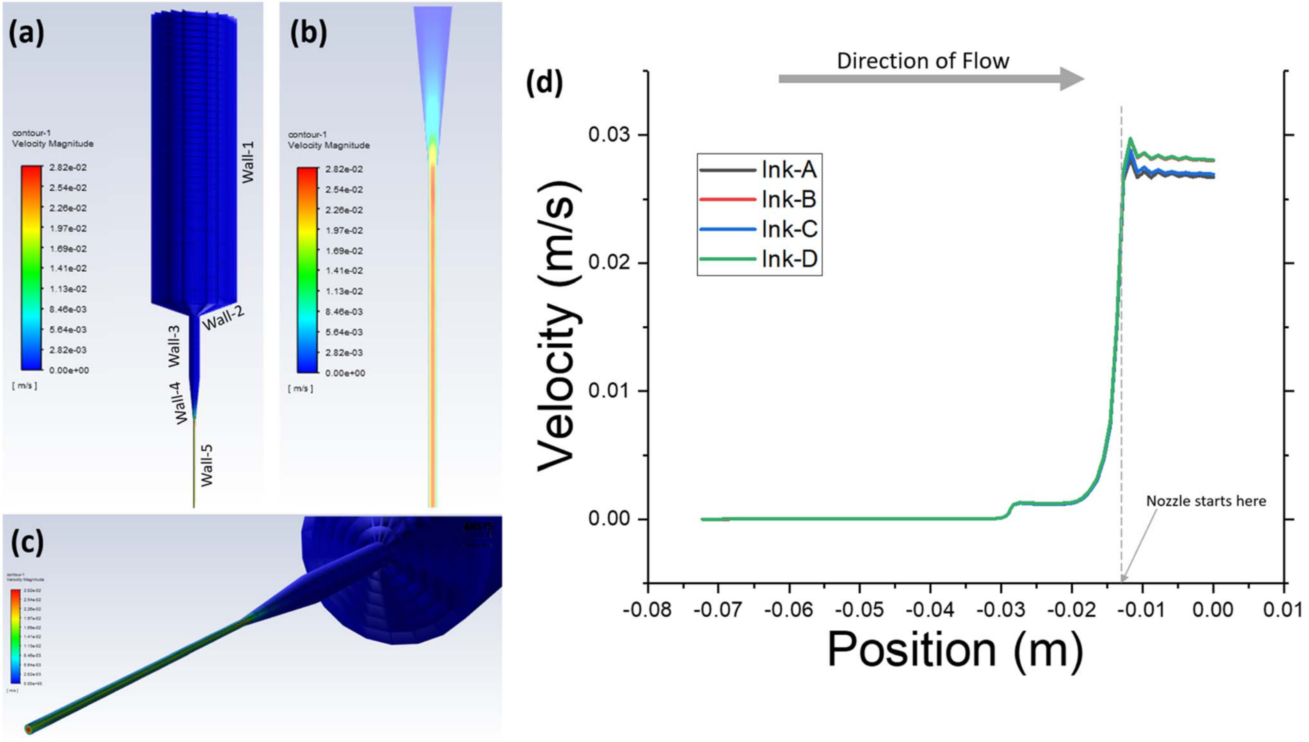

Fig. 15 (a) Velocity profile for ink-A using ANSYS fluent, (b) development of laminar flow within the nozzle, and (c) developed velocity profile at the nozzle outlet. (d) Velocity *versus* position plot along for all the hydrogel inks, generated using CFD simulations in ANSYS fluent.

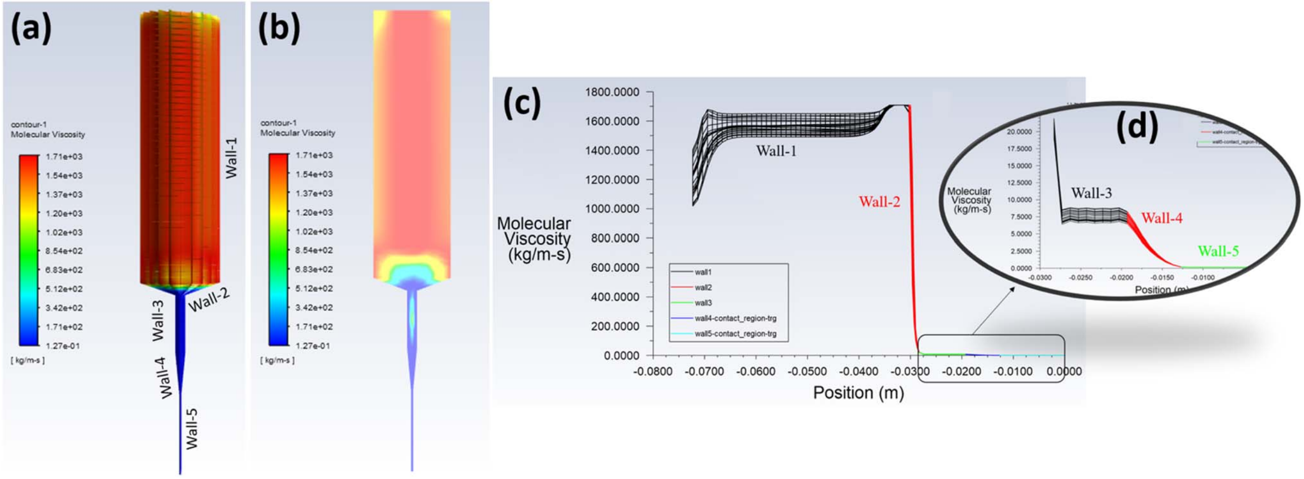

Fig. 16 (a) Viscosity profile of ink-A using CFD simulations, (b) 2D representation of the viscosity profile. (c) Viscosity *versus* position plot along the wall surface for ink-A, generated using CFD simulations in ANSYS fluent. (d) Zoomed-in view highlighting the lower viscosity regions within the converging section of the geometry.

hydrogel layer stationary. The adjacent layers begin to move, creating velocity gradients that result in shear stress. This shear reduces the viscosity of the ink near the wall. As we move toward the center of the flow channel, the influence of the wall diminishes, the shear stress reduces, and the viscosity correspondingly increases. This results in higher viscosity values in the central region compared to the regions near the wall. When the hydrogel ink enters the nozzle region, the available flow area is significantly reduced, which enhances the influence of the wall. This leads to increased shear stress, resulting in a substantial decrease in the viscosity of the hydrogel ink, which is consistent with the findings of Raj *et al.* (2022).[59] This decrease in viscosity facilitates the proper extrusion of hydrogel inks through the nozzle during the 3D printing.

Fig. 16(c) presents the viscosity *versus* position plots from ANSYS fluent, illustrating the viscosity distribution near the wall regions for ink-A. The plot reveals a continuous decrease in viscosity along the wall surface as the hydrogel ink moves from the syringe barrel toward the nozzle outlet. Notably, this change in viscosity is primarily observed in the converging sections (wall-2 and wall-4), whereas the viscosity remains relatively constant in regions with a uniform cross-section. A similar profile was also observed for the other hydrogel inks as shown in Fig. S8 (SI).

Simulated shear stress profile. From the CFD simulations, we can observe that the shear stress values are high near the walls, and they decrease significantly as we move toward the center of the syringe. As shown in Fig. 17(a)–(c), the shear stress within the geometry is predominantly concentrated in the nozzle region, while the syringe section experiences relatively low shear stress, consistent with the profiles reported by Chand *et al.*[34] This is due to the larger cross-sectional area in the syringe, which minimizes wall effects. However, as the hydrogel passes through the geometry and enters the region enclosed by wall-3, the shear stress becomes noticeably high. This is because of the sudden reduction in cross-sectional area, which significantly enhances the influence of the wall. Since the cross-sectional area remains constant within the wall-3 region, the shear stress also becomes constant within this region. As the hydrogel flows further into the converging region enclosed by wall-4, the continuously narrowing cross-section causes a steady rise in shear stress. Upon reaching wall-5, located at the entrance of the cylindrical nozzle, the shear stress reaches its maximum value and remains nearly constant throughout the nozzle length until the outlet.

Fig. 17(d) shows the shear stress *versus* position plot along the regions near the wall for ink-A, illustrating how shear stress varies as the hydrogel travels from the syringe barrel to the nozzle outlet. It is evident that shear stress increases significantly within the converging sections of the geometry, while remaining nearly constant in regions with a uniform cross-section. The highest shear stress of approximately 90 Pa is observed in the nozzle region, mainly due to its narrow cross-section, which increases the effect of the wall and ultimately leads to a rise in shear stress. A similar trend was observed for the other hydrogel inks as well. As shown in Fig. S10 (SI), the highest shear stress experienced by ink-B is 218 Pa, ink-C 83 Pa and ink-D is 186 Pa. This correlates to the simulated and experimental pressures listed in Table 3 with the largest pressure required to extrude is for ink-B followed by ink-D, ink-A and ink C.

This type of quantitative analysis provides valuable insights into the distribution of shear stress within a particular nozzle, which can be utilized to optimize nozzle designs for specific applications.[34] For the bioprinting of cellular scaffolds, shear stress within the nozzle plays a critical role in determining cell viability because the high shear rates are known to adversely affect cell survival.[60] Another study by Nair *et al.* showed that when cells are subjected to high shear rates in narrow nozzles, their viability drops because of membrane damage.[61] Blaeser *et al.* further demonstrated that cell survival decreases progressively with increasing shear stress during extrusion, and

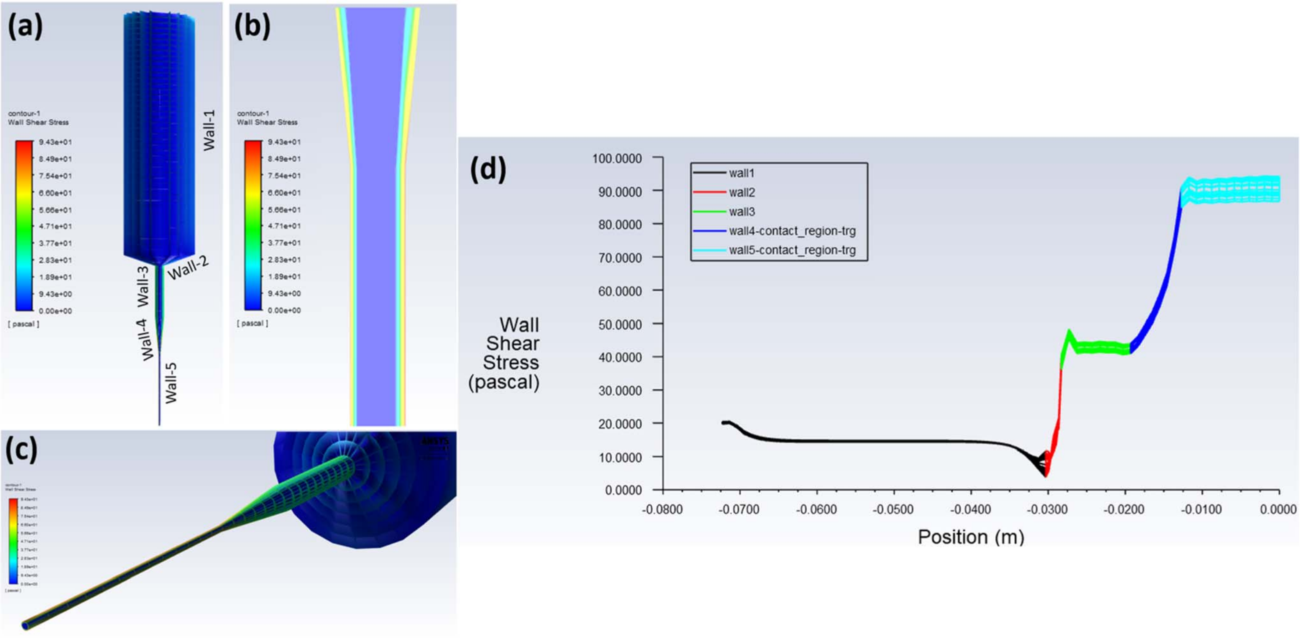

Fig. 17 (a) Shear stress profile for ink-A obtained from CFD simulations, (b) 2D cross-sectional view illustrating shear stress distribution within the nozzle, and (c) schematic depiction of the progressive increase in shear stress as the hydrogel ink flows through different sections of the syringe–nozzle geometry. (d) Shear stress *vs.* position plot along the wall surface for ink-A, generated using CFD simulations in ANSYS fluent.

that beyond a certain threshold, the loss in viability becomes significant.[62] Ribeiro *et al.* added that it is not only the magnitude of shear stress but also the duration of exposure that influences how cells behave after printing, including their ability to proliferate and differentiate.[63] These findings underline the importance of considering shear conditions when designing bioinks. For κCG inks, which otherwise show favorable rheological behavior for extrusion, the key challenge will be to maintain extrusion pressures and shear stresses at levels that do not compromise cell integrity. Linking rheology, processing parameters, and biological response is therefore critical for advancing their use in biofabrication.

Simulated shear rate profile. As can be seen in Fig. 18(a)–(c), the shear rate is highest near the nozzle wall and decreases toward the center. When the hydrogel passes through the converging region inside the nozzle, the shear rate increases, contributing to the shear-thinning effect and promoting stable extrusion.

From the shear rate *versus* position plots along the central axis for all hydrogel inks, shown in Fig. 18(d), it is evident that the shear rate begins to increase significantly as the cross-sectional area of the geometry decreases. This trend is particularly noticeable just before the hydrogel enters the nozzle, where the converging section (wall-4) causes a sharp rise in shear rate, peaking at the nozzle inlet. However, once the ink reaches the nozzle, characterized by a uniform cross-section, the shear rate at the central axis begins to decrease substantially. This is attributed to the establishment of a steady laminar flow profile within the nozzle, where the layers of the hydrogel move more smoothly relative to each other, in contrast to the more turbulent conditions in the converging region. We can also observe a smaller peak near position −0.03 m, right above the nozzle, which aligns with the narrowing geometry at wall-2 and wall-3, highlighting how even slight constrictions in the path can influence local shear conditions.

This quantitative insight into shear rate values allows for more informed experimental design, particularly for the thixotropy experiments. Traditionally, these experiments were conducted by arbitrarily varying shear rates across a wide range.[43] However, the use of CFD simulations enables the modification of this conventional protocol by incorporating shear rates that are representative of those observed during actual printing.

Analysis of flow profiles at the syringe inlet and nozzle outlet. As we have already examined the overall profiles of various parameters associated with the extrusion printing of hydrogels, we now focus on visualizing these properties, specifically at the syringe inlet and the nozzle outlet. Fig. 19(a) presents the pressure profile at both the entrance and exit of the geometry. The results clearly indicate that the pressure is highest at the syringe inlet and lowest at the nozzle outlet, with negligible radial variation. Fig. 19(b) shows the corresponding velocity profiles. At the inlet, the velocity is relatively low due to the larger cross-sectional area, while a significantly higher velocity is observed at the outlet. The outlet velocity profile confirms a fully developed laminar flow, characterized by the highest velocity along the central axis, which gradually decreases toward the walls and eventually drops to zero due to the no-slip boundary condition. The viscosity distribution, shown in Fig. 19(c), reflects the effects of shear-thinning behavior. At the inlet, the viscosity shows minor variation, with lower values near the central region and higher values near

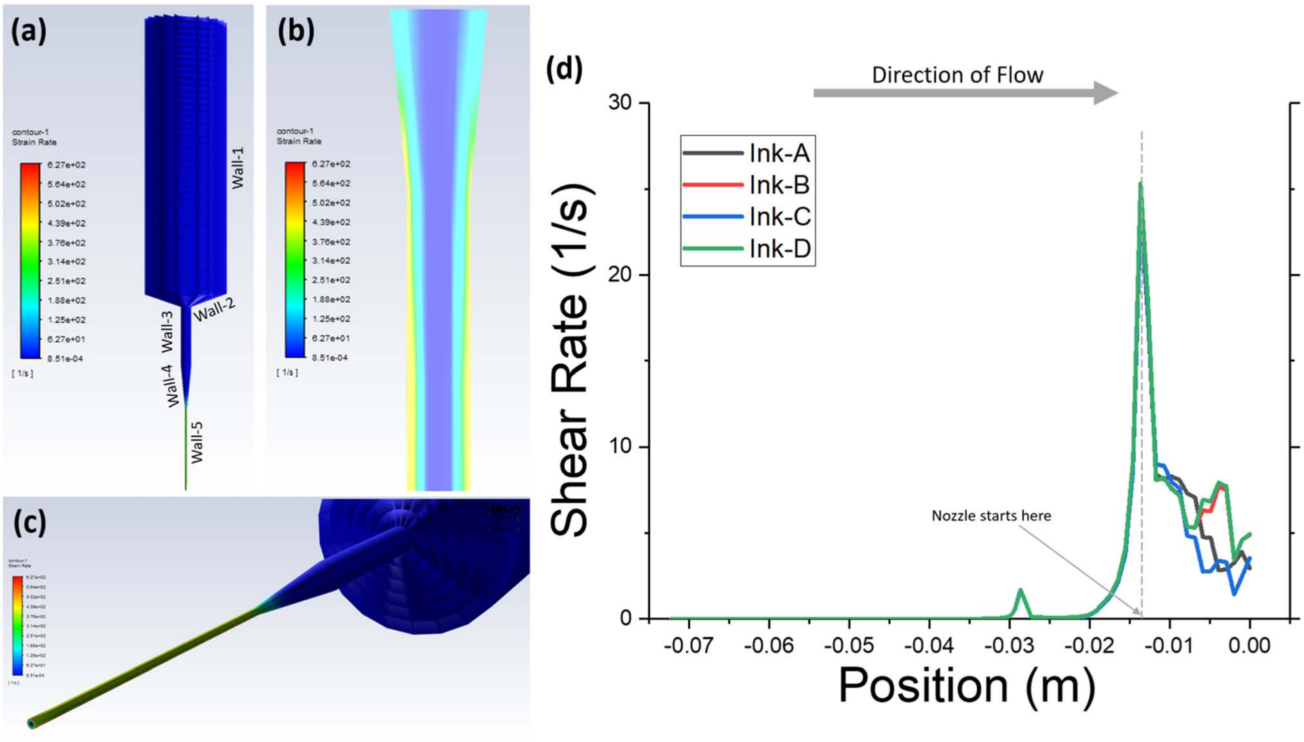

Fig. 18 Shear rate profile for ink-A obtained from CFD simulations, (b) 2D cross-sectional view illustrating shear rate distribution within the nozzle, and (c) schematic depiction of the progressive increase in shear rate as the hydrogel ink flows through different sections of the syringe–nozzle geometry. (d) Shear rate *versus* position plot for all the hydrogel inks, generated using CFD simulations in ANSYS fluent.

the wall, attributable to shear stress induced by wall interaction. At the outlet of the nozzle, the viscosity becomes very low due to the high shear rates present within the nozzle.

Since shear stress and shear rate are nonlinearly related, they tend to exhibit similar spatial profiles during flow, as shown in Fig. 19(d) and (e). At the syringe inlet, both quantities show slight variation near the walls but remain relatively uniform near the central axis. In contrast, at the nozzle outlet, a significant gradient is observed, with the highest values occurring near the nozzle walls. These values gradually decrease toward the center, reflecting the strong shear developed due to the confined geometry and high velocity gradients near the wall.

Thixotropy of hydrogel inks

From the CFD analysis of shear rates in the regions near the walls for ink-A, we can observe that the shear rate begins to peak in the converging zone just before the nozzle (wall-4), reaching a maximum value that then remains constant along the nozzle wall, as shown in Fig. 20(a). A similar trend is observed for the other hydrogel inks as well. The shear rate values in the syringe

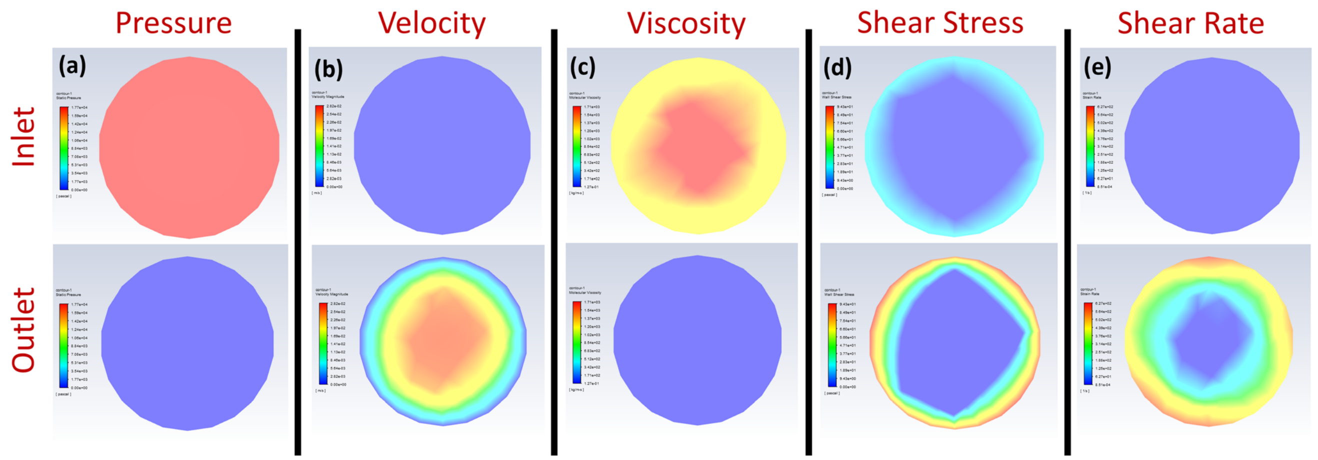

Fig. 19 2D profiles for ink-A at inlet (upper) and outlet (lower) for (a) pressure, (b) velocity, (c) viscosity, (d) shear stress, and (e) shear rate.

barrel region are relatively low and gradually increase as we move toward the nozzle. To visualize shear rate variations across the geometry, zoomed-in plots for selected regions are shown in Fig. 20(b) and (d). The constant segments in these plots correspond to sections with uniform cross-section, and shear rate values from these regions were used to design the modified thixotropic protocol. Specifically, wall-1 experienced a shear rate of 0.01 s^{-1}, wall-3 experienced 5 s^{-1}, and wall-5 experienced 500 s^{-1}. Similar shear rate variation is shown by all inks as shown in Fig. S11 (SI). This approach enhances the relevance of the experimental conditions, potentially leading to more meaningful and accurate results.

From Fig. 21, it can be seen that all the hydrogel inks show good viscosity recovery as soon as the applied shear is removed. For ink-A, the average viscosity at the initial shear rate of 0.01 s^{-1} is 936.4 Pa s, which reduces as we move to the intermediate and high shear rate intervals. As soon as the shear rate is reduced back to 0.01 s^{-1}, the hydrogel begins to regain its viscosity, and ultimately reaches 804.1 Pa s after 90 seconds. This gives the viscosity recovery of 85% for ink-A. Similarly, for ink-C, the viscosity recovery is 79%. This loss in viscosity values of the hydrogel inks is because the applied shear destroyed the physical bonds that exist among the macromolecules in the hydrogels, and they require a longer period of time for their reconstruction.[64] As can be seen from the literature, the viscosity recovery for a good printable hydrogel ink is around 80 to 85%,[38,43,49] our inks also show similar results. Hence, we can say that our hydrogel inks can be effectively used for various 3D printing applications.

Ink-B and ink-D exhibit viscosity recoveries of 57% and 62%, respectively. These values are comparatively lower, which can be attributed to sample slippage during the high shear rate phase (500 s^{-1}) of the thixotropy test. At such high shear rates, a portion of the hydrogel ink tends to slip out of the rheometer geometry, leading to a reduced sample volume for measurement. As a result, the final viscosity recorded during the second low shear rate interval (0.01 s^{-1}) appears lower than expected, subsequently underestimating the viscosity recovery. Interestingly, despite these low recovery values, both ink-B and ink-D demonstrate excellent structure retention during actual 3D printing of multi-layer constructs, which inherently requires a high viscosity recovery. This discrepancy is due to the fact that there is sample slipping out the geometry, due to which the true viscosity of the hydrogel cannot be measured.

To gain a deeper understanding of sample slippage, the shear stress profiles from Fig. 21 can be analyzed. Ideally, for non-Newtonian fluids such as the κCG hydrogel inks used in this study, shear stress increases nonlinearly with increasing shear rate, a characteristic feature of shear-thinning behavior. For ink-A and ink-C, this nonlinear relationship is evident, with a sharp and sustained rise in shear stress observed as the shear rate increases, which remains consistent within each interval until the shear rate is altered. However, for ink-B and ink-D, the transition from the intermediate shear rate (5 s^{-1}) to the high shear rate (500 s^{-1}) does not produce a substantial increase in shear stress. The expected sharp rise is absent, suggesting significant sample slippage at higher shear rates. Due to the slipping, the effective volume of the sample under stress decreases, resulting in a decrease in the measured shear stress and, consequently, the apparent viscosity. As a result, no distinct shear stress peaks are observed for ink-B and ink-D

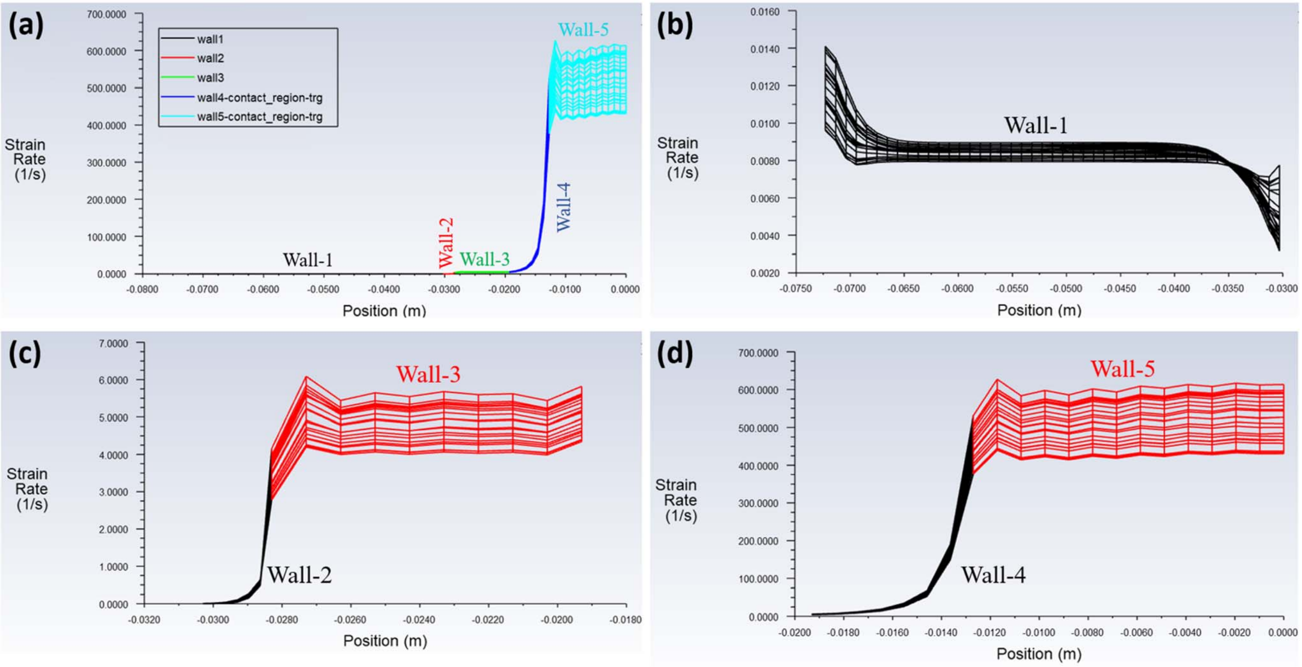

Fig. 20 (a) Shear rate *vs.* position plot along the wall surface for ink-A, generated using CFD simulations in ANSYS fluent. Zoomed-in views of specific regions for: (b) wall-1, (c) wall-2 & wall-3, and (d) wall-4 & wall-5.

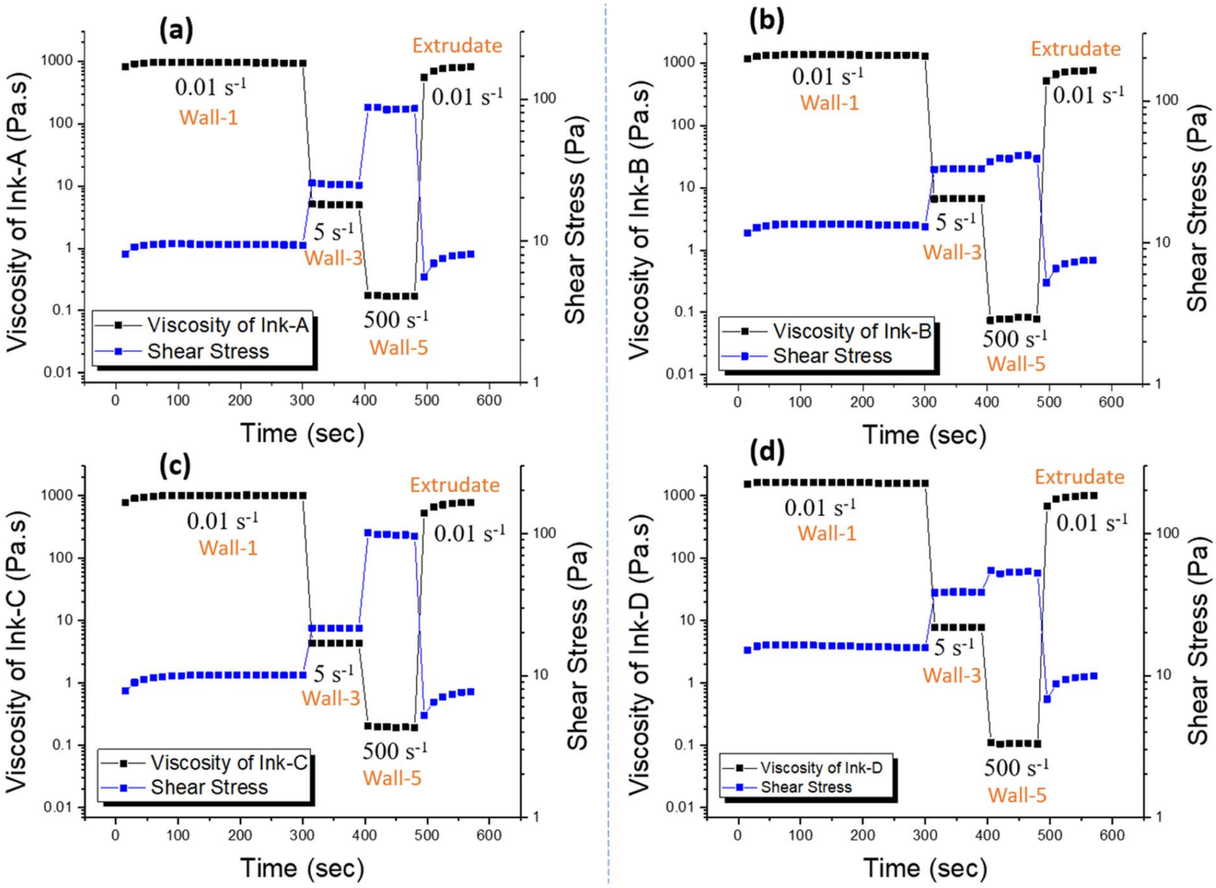

Fig. 21 Thixotropic results, along with the respective shear stress curve for (a) ink-A, (b) ink-B, (c) ink-C, and (d) ink-D.

during this transition, further confirming the presence of slippage.

Conclusion

This study presents a comprehensive evaluation of κCG based hydrogel inks for extrusion-based 3D printing, incorporating rheological characterization, printing trials, and CFD simulations. Variations in the ink composition, including the addition of 10 mM KCl and AuNPs, enabled a comparative assessment of printability and structural fidelity. All formulations exhibited shear-thinning behavior, as observed from the flow curves, and were subsequently characterized using the Power Law model to extract flow indices. Oscillatory stress sweep measurements showed higher G' for ink-B and ink-D due to the presence of KCl, indicating enhanced mechanical strength, whereas ink-A and ink-C exhibited comparatively lower G' values. All hydrogel inks demonstrated yield stress values between 18 and 26 Pa, confirming their potential suitability for 3D printing by enabling structural retention during and after extrusion.

Single-layer printing was optimal in hydrogel inks without KCl salt, with ink-A showing the highest printability, whereas KCl-crosslinked inks offered superior multi-layer stability. Ink-D, containing both KCl and AuNPs, demonstrated the best multi-layer printability by combining the mechanical stability due to KCl crosslinking and enhanced shear-thinning effect due to the addition of AuNPs. CFD simulations helped visualize flow dynamics and estimate extrusion pressures, revealing spatial variations in shear rate and viscosity, particularly in the converging nozzle region. While simulated pressures were lower than experimental values, these CFD simulations provided practical estimates for initial printing parameters. It is important to note that the CFD model does not account for factors such as friction between the hydrogel and the walls of syringe–nozzle geometry, interactions between successive layers of the hydrogel ink, or the influence of AuNPs and their potential interactions with the hydrogel as well as with other nanoparticles. These assumptions help to simplify the model and make the complex calculations easier, faster, and computationally less expensive. Simulation-informed thixotropy tests showed high viscosity recovery in hydrogel inks without KCl salt, while KCl-crosslinked inks exhibited lower values, likely due to sample slippage at high shear rates leading to underestimation. Nonetheless, the crosslinked inks demonstrated effective structural recovery during the printing.

Overall, this integrated approach advances the understanding of κCG hydrogels for biomedical printing. Future studies could build on this work by incorporating multiphase or transient models to better capture particle–matrix interactions and their influence on flow behavior. Further efforts may also focus on cell-laden formulations, evaluation of biocompatibility, and refinement of CFD models to account for viscoelasticity and dynamic printing conditions, thereby improving predictive capability and supporting real-world applications.

Author contributions

Siraj Ahmad: experiments, data analysis, simulations, writing. Hatif Alam: characterization, thermal analysis, rheology, writing. Prachi Thareja: conceptualization, review, writing, supervision, project management, and funding acquisition.

Conflicts of interest

There are no conflicts to declare.

Data availability

Datasets will be made available on request.

Supplementary information is available. See DOI: **https://doi.org/10.1039/d5ra04380h**.

Acknowledgements

Prachi Thareja acknowledges the funding received from CSIR under grant number 22WS(049)/2023-24//EMR-II/ASPIRE. We also acknowledge DST-FIST FTIR facility. For help with writing, we asked Grammarly to respond to these AI prompts: prompts created by Grammarly – "Improve it".

References

1 M. S. Bindu and I. A. Levine, *J. Appl. Phycol.*, 2011, **23**, 789–796.

2 V. L. Campo, D. F. Kawano, D. B. da Silva and I. Carvalho, *Carbohydr. Polym.*, 2009, **77**, 167–180.

3 J. Necas and L. Bartosikova, *Vet. Med.*, 2013, **58**, 187–205.

4 N. Rhein-Knudsen, M. T. Ale and A. S. Meyer, *Mar. Drugs*, 2015, **13**, 3340–3359.

5 N. González-Ballesteros, M. D. Torres, N. Flórez-Fernández, L. Diego-González, R. Simón-Vázquez, M. C. Rodríguez-Argüelles and H. Domínguez, *Int. J. Biol. Macromol.*, 2021, **183**, 1436–1449.

6 X. Chen, X. Zhao, Y. Gao, J. Yin, M. Bai and F. Wang, *Mar. Drugs*, 2018, **16**, DOI: **10.3390/md16080277**.

7 S. A. Razack, Y. E. Kim and H. W. Kang, *Int. J. Biol. Macromol.*, 2025, **291**, 138974.

8 N. Das, Vikas, A. Kumar, S. Soni and R. G. Rayavarapu, *Beilstein J. Nanotechnol.*, 2024, **15**, 678–693.

9 A. M. Salgueiro, A. L. Daniel-da-Silva, S. Fateixa and T. Trindade, *Carbohydr. Polym.*, 2013, **91**, 100–109.

10 A. Pourjavadi, M. Doroudian, A. Ahadpour and S. Azari, *Int. J. Biol. Macromol.*, 2019, **126**, 310–317.

11 M. Garg, P. Patel and P. Thareja, *Microchem. J.*, 2023, **194**, 109241.

12 S. Swarupa and P. Thareja, *Int. J. Biol. Macromol.*, 2024, **266**, 131104.

13 K. Loukelis, D. Papadogianni and M. Chatzinikolaidou, *Int. J. Biol. Macromol.*, 2022, **209**, 1720–1730.

14 S. Distantina, R. Rochmadi, M. Fahrurrozi and W. Wiratni, *Eng. J.*, 2013, **17**, 57–66.

15 D. Seliktar, *Science*, 2012, **336**, 1124–1128.

16 B. Neamtu, A. Barbu, M. O. Negrea, C. Ștefan Berghea-Neamțu, D. Popescu, M. Zăhan and V. Mireșan, *Int. J. Mol. Sci.*, 2022, **23**, 9117.

17 S. G. Marapureddy and P. Thareja, in *Biointerface Engineering: Prospects in Medical Diagnostics and Drug Delivery*, Springer Singapore, Singapore, 2020, pp. 75–99.

18 E.-M. Pacheco-Quito, R. Ruiz-Caro and M.-D. Veiga, *Mar. Drugs*, 2020, **18**, 583.

19 M. Sathuvan, R. Thangam, M. Gajendiran, R. Vivek, S. Balasubramanian, S. Nagaraj, P. Gunasekaran, B. Madhan and R. Rengasamy, *Carbohydr. Polym.*, 2017, **160**, 184–193.

20 G. R. Bardajee, Z. Hooshyar and F. Rastgo, *Colloid Polym. Sci.*, 2013, **291**, 2791–2803.

21 E. M. Ahmed, *J. Adv. Res.*, 2015, **6**, 105–121.

22 D. Almeida, F. Küppers, A. Gusmão, A. C. Manjua, C. F. R. Ferreira, C. A. M. Portugal, J. C. Silva, P. Sanjuan-Alberte and F. C. Ferreira, *J. Mater. Sci.*, 2024, **59**, 14573–14592.

23 M.-A. Kamlow, F. Spyropoulos and T. Mills, *Food Hydrocolloids Health*, 2021, **1**, 100044.

24 P. Patel, K. Mujmer, V. K. Aswal, S. Gupta and P. Thareja, *Mater. Today Commun.*, 2023, **35**, DOI: **10.1016/j.mtcomm.2023.105807**.

25 C. Stavarache, S. A. Gârea, A. Serafim, E. Olăreț, G. M. Vlăsceanu, M. M. Marin and H. Iovu, *Polymers*, 2024, **16**, 305.

26 S. Kumari, P. Mondal and K. Chatterjee, *Carbohydr. Polym.*, 2022, **290**, 119508.

27 N. Paxton, W. Smolan, T. Böck, F. Melchels, J. Groll and T. Jungst, *Biofabrication*, 2017, **9**, 044107.

28 J. Malda, J. Visser, F. P. Melchels, T. Jüngst, W. E. Hennink, W. J. A. Dhert, J. Groll and D. W. Hutmacher, *Adv. Mater.*, 2013, **25**, 5011–5028.

29 A. Schwab, R. Levato, M. D'Este, S. Piluso, D. Eglin and J. Malda, *Chem. Rev.*, 2020, **120**, 11028–11055.

30 A. Malekpour and X. Chen, *J. Funct. Biomater.*, 2022, **12**, 40.

31 J. Wang, Z. Cui and M. Maniruzzaman, *Int. J. Pharm.*, 2023, **640**, DOI: **10.1016/j.ijpharm.2023.123020**.

32 U. N. M. Fareez, S. A. A. Naqvi, M. Mahmud and M. Temirel, *Adv. Healthcare Mater.*, 2024, **13**, DOI: **10.1002/adhm.202400643**.

33 R. Hajili and M. Temirel, *Bitlisfen*, 2024, **13**, 1233–1246.

34 R. Chand, B. S. Muhire and S. Vijayavenkataraman, *Int. J. Bioprint.*, 2022, **8**, 45–60.

35 I. Diañez, C. Gallegos, E. Brito-de la Fuente, I. Martínez, C. Valencia, M. C. Sánchez, M. J. Diaz and J. M. Franco, *Food Hydrocolloids*, 2019, **87**, 321–330.

36 H. Wan, Z. Liu, Q. He, D. Wei, S. Mahmud and H. Liu, *Int. J. Biol. Macromol.*, 2021, **176**, 282–290.

37 Y. Agarwal, P. S. Rajinikanth, S. Ranjan, U. Tiwari, J. Balasubramnaiam, P. Pandey, D. K. Arya, S. Anand and P. Deepak, *Int. J. Biol. Macromol.*, 2021, **176**, 376–386.

38 P. Thareja, S. Swarupa, S. Ahmad and M. E. Jinugu, *Curr. Opin. Colloid Interface Sci.*, 2025, **77**, 101918.

39 K. M. Albano, C. M. L. Franco and V. R. N. Telis, *Food Hydrocolloids*, 2014, **40**, 30–43.

40 E. Reina-Romo, S. Mandal, P. Amorim, V. Bloemen, E. Ferraris and L. Geris, *Front. Bioeng. Biotechnol.*, 2021, **9**, DOI: **10.3389/fbioe.2021.701778**.

41 P. Bertsch, M. Diba, D. J. Mooney and S. C. G. Leeuwenburgh, *Chem. Rev.*, 2023, **123**(2), 834–873.

42 Y. Zhu, W. Di, M. Song, B. Chitrakar and Z. Liu, *J. Food Eng.*, 2023, **340**, DOI: **10.1016/j.jfoodeng.2022.111316**.

43 J. H. Teoh, F. T. Abdul Shakoor and C. H. Wang, *Pharm. Res.*, 2022, **39**, 281–294.

44 T. M. Oyinloye and W. B. Yoon, *Processes*, 2022, **10**, DOI: **10.3390/pr10010068**.

45 V. K. Konaganti, M. Ansari, E. Mitsoulis and S. G. Hatzikiriakos, *J. Non-Newtonian Fluid Mech.*, 2015, **225**, 94–105.

46 E. Mitsoulis and S. G. Hatzikiriakos, *Int. Polym. Process.*, 2012, **27**, 535–546.

47 P. A. Amorim, M. A. d'Ávila, R. Anand, P. Moldenaers, P. Van Puyvelde and V. Bloemen, *Bioprinting*, 2021, **22**, e00129.

48 R. Agrawal and E. Garcia-Tunon, *Soft Matter*, 2024, **20**, 7429–7447.

49 Y. Jiang, J. Zhou, C. Feng, H. Shi, G. Zhao and Y. Bian, *J. Mater. Sci.*, 2020, **55**, 15709–15725.

50 M. Dinkgreve, J. Paredes, M. M. Denn and D. Bonn, *J. Non-Newtonian Fluid Mech.*, 2016, **238**, 233–241.

51 A. L. Daniel-Da-Silva, A. B. Lopes, A. M. Gil and R. N. Correia, *J. Mater. Sci.*, 2007, **42**, 8581–8591.

52 J. I. Renaka, W. Setyaningsih and M. Palma, *Food Chem.*, 2025, **495**, DOI: **10.1016/j.foodchem.2025.146371**.

53 J. Jamaludin, F. Adam, R. A. Rasid and Z. Hassan, *Thermal Studies on Arabic Gum-Carrageenan Polysaccharides Film*, 2017, vol. 19.

54 T. R. Thrimawithana, S. Young, D. E. Dunstan and R. G. Alany, *Carbohydr. Polym.*, 2010, **82**, 69–77.

55 S. Boularaoui, A. Shanti, M. Lanotte, S. Luo, S. Bawazir, S. Lee, N. Christoforou, K. A. Khan and C. Stefanini, *ACS Biomater. Sci. Eng.*, 2021, **7**, 5810–5822.

56 M. S. Marques, K. M. Zepon, J. M. Heckler, F. D. P. Morisso, M. M. da Silva Paula and L. A. Kanis, *Int. J. Biol. Macromol.*, 2019, **124**, 838–845.

57 C. Guo, M. Zhang and H. Chen, *Int. J. Food Sci. Technol.*, 2021, **56**, 2264–2272.

58 E. N. Nikolaou, E. Apostolidis, E. K. Nikolidaki, E. D. Karvela, A. Stergiou, T. Kourtis and V. T. Karathanos, *Gels*, 2025, **11**, 574.

59 R. Raj, S. Vamsi Venkata Krishna, A. Desai, C. Sachin and A. R. Dixit, *IOP Conf. Ser.: Mater. Sci. Eng.*, 2022, **1225**, 012009.

60 Y. Sriphutkiat, S. Kasetsirikul, D. Ketpun and Y. Zhou, *Sci. Rep.*, 2019, **9**, 17774.

61 K. Nair, M. Gandhi, S. Khalil, K. C. Yan, M. Marcolongo, K. Barbee and W. Sun, *Biotechnol. J.*, 2009, **4**, 1168–1177.

62 A. Blaeser, D. F. Duarte Campos, U. Puster, W. Richtering, M. M. Stevens and H. Fischer, *Adv. Healthcare Mater.*, 2016, **5**, 326–333.

63 A. Ribeiro, M. Blokzijl, R. Levato, C. Visser, M. Castilho, T. Vermonden, J. Malda and J. Malda, *Biofabrication*, 2017, **10**, 014102.

64 Y. Yang, X. Xie, Z. Yang, X. Wang, W. Cui, J. Yang and Y.-W. Mai, *Macromolecules*, 2007, **40**, 5858–5867.